Physica D 241 (2012) 1421–1440

Contents lists available at SciVerse ScienceDirect

Physica D

journal homepage: www.elsevier.com/locate/physd

On sequential data assimilation for scalar macroscopic traffic flow models

Sébastien Blandin [a,*], Adrien Couque [b], Alexandre Bayen [c,a], Daniel Work [d]

[a] IBM Research Collaboratory – Singapore, Singapore

[b] California Center for Innovative Transportation, United States

[c] Systems Engineering, Department of Electrical Engineering and Computer Sciences, University of California, Berkeley, United States

[d] Department of Civil and Environmental Engineering, University of Illinois at Urbana-Champaign, United States

ARTICLE INFO

Article history:
Received 30 August 2011
Received in revised form
12 April 2012
Accepted 14 May 2012
Available online 22 May 2012
Communicated by H.A. Dijkstra

Keywords:
Traffic flow
Macroscopic modeling
Sequential estimation
Data assimilation
Conservation law
Riemann problem

ABSTRACT

We consider the problem of sequential data assimilation for transportation networks using optimal filtering with a scalar macroscopic traffic flow model. Properties of the distribution of the uncertainty on the *true state* related to the specific nonlinearity and non-differentiability inherent to macroscopic traffic flow models are investigated, derived analytically and analyzed. We show that nonlinear dynamics, by creating discontinuities in the traffic state, affect the performances of classical filters and in particular that the distribution of the uncertainty on the traffic state at shock waves is a mixture distribution. The non-differentiability of traffic dynamics around stationary shock waves is also proved and the resulting optimality loss of the estimates is quantified numerically. The properties of the estimates are explicitly studied for the Godunov scheme (and thus the Cell-Transmission Model), leading to specific conclusions about their use in the context of filtering, which is a significant contribution of this article. Analytical proofs and numerical tests are introduced to support the results presented. A Java implementation of the classical filters used in this work is available on-line at http://traffic.berkeley.edu for facilitating further efforts on this topic and fostering reproducible research.

1. Introduction

1.1. Motivation

At the age of ubiquitous sensing, scientists and engineers are faced with the challenge of leveraging massive cross-domain datasets to solve increasingly complex problems and address systemic issues at unprecedented scales [1]. In transportation networks, the spread of crowd-sourced traffic data is revolutionizing traffic data collection. In parallel, the democratization of publicly available and easily accessible high performance computing resources offers scalable tools for massive data processing. This conjunction of factors is accelerating the pace of development and implementation of novel on-line traffic estimation methods and filtering algorithms, from which real-time congestion control strategies may be designed at the scale of mega-cities.

The theory of *estimation* is concerned with the problem of providing statistics of a process state, based on measurements and a priori knowledge. The a priori knowledge of the process often consists of a parametric *model*, which approximately describes the process behavior mathematically. The definition of a *loss function* allows for the formulation of the estimation problem as an optimization problem and the identification of certificates of optimality. When the estimated quantities are not directly observed, (so-called *latent variables*) the estimation problem is referred to as an *inverse problem* [2]. For physical systems, the estimation problem, or *data assimilation* problem [3,4], is solved using a data assimilation algorithm, which combines optimally, in the sense of the loss function, the a priori knowledge of the system, and the observations from the system. In particular, a *filtering* algorithm provides the solution to an inverse problem which includes the additional constraint that, for all times t, only observations at or before time t can be used to compute estimates at time t.

The basis for modern filtering theory was set by Kalman in 1960 who introduced a sequential filtering algorithm for linear dynamical systems, the *Kalman filter* (KF) [5]. This algorithm extended the work of Wiener [6] and proposed one of the first results on optimal filtering for linear dynamical systems with non-stationary statistics. The KF *sequentially* computes the best estimate of the *true state* of a system from combined knowledge of a model and observations. The KF has been widely applied by the control community, notably to signal processing, sensor data fusion, navigation and guidance [7,8].

* Correspondence to: IBM Singapore Pte Ltd, 9 Changi Business Park Central 1, The IBM Place, Singapore 486048, Singapore.

E-mail addresses: sblandin@sg.ibm.com (S. Blandin), adrien.couque@polytechnique.org (A. Couque), bayen@berkeley.edu (A. Bayen), dbwork@illinois.edu (D. Work).

0167-2789/$ – see front matter © 2012 Elsevier B.V. All rights reserved.
doi:10.1016/j.physd.2012.05.005

In the meteorology community, the estimation problem for nonlinear systems has been heavily studied, with subsequent development of sophisticated data assimilation techniques [3,4], which fall into two major categories: *variational methods* and *optimal interpolation* methods. Variational methods [4] consist of finding the solution of a model (with or without stochastic forcing) which minimizes a certain distance to observations. In meteorology, a common formulation is the 3D-Var algorithm [9] for the static problem and 4D-Var algorithm in the time-varying case [10].

The need for solving the inverse problem for increasingly complex systems, for which the classical assumptions of linearity of the dynamics and normality of the error terms break, has motivated the development of *suboptimal* sequential estimation algorithms. Suboptimal sequential estimation algorithms, reviewed in Sections 2.2 and 2.3, can be derived from the KF by different types of methods:

1. *Deterministic filters*: *extended Kalman filter* (EKF) [11], *unscented Kalman filter* (UKF) [12].
2. *Stochastic filters*: *ensemble Kalman filter* (EnKF) [13], *particle filter* (PF) [14].

For traffic applications, it is also important to mention the *mixture Kalman filter* (MKF) [15], which provides optimality guarantees for *conditionally linear* systems. A comprehensive review of the application of data assimilation algorithms in the transportation community can be found in the following section.

1.2. Sequential estimation for transportation networks

Sequential traffic state estimation dates back to the 1970s and the work of Gazis [16,17], who independently used the KF and the EKF to estimate traffic density in the Lincoln tunnel, New York, for the purpose of traffic control. More recent work from Papageorgiou [18,19] involves the application of the EKF to a non-scalar traffic model [20]. The EKF has also been applied [21] to the LWR equation with a Smulders [22] flux function.

The MKF [15] is an extension of the KF to conditionally linear dynamical systems. The MKF has been applied in the transportation community [23–25] to the *cell-transmission model* (CTM) [26,27], which exhibits piecewise linear dynamics, conditioned on the phases of traffic (free-flow, congestion) upstream and downstream.

In recent years, *sequential Monte Carlo* methods, or PF, and so-called *ensemble methods* such as the EnKF have been applied to traffic estimation [28,29]. Ensemble methods [13] consist of representing the first moment of the state estimate distribution by a set of samples and using a linear measurement update, whereas particle methods [30] consist in propagating a sample representation of the full distribution of the estimate and using a nonlinear measurement update.

Another notable filter is the UKF [12] which introduces an *unscented transformation* providing an exact representation of the first two moments of a distribution by a set of deterministically determined samples (see [31] for a traffic application).

A variety of traffic models and filters have been shown to perform well for practical applications. However, the problem of the structural limits of data assimilation algorithms for traffic estimation has not received much attention. It is well known that, in practice, high accuracy can be achieved with sufficiently accurate measurements in sufficiently large volumes. But with massive datasets coming from increasingly diverse sources, traceability and high quality of traffic data are not necessarily guaranteed. Being able to identify the estimation errors inherent to the structure of traffic phenomena is required for the design of more robust, transparent data assimilation algorithms, and scalable, appropriate data collection methodologies.

In this article, we propose to analyze the structural properties of one of the most classical macroscopic traffic flow models, the *Lighthill–Whitham–Richards* (LWR) *partial differential equation* (PDE) [32,33], in the context of estimation. We present the difficulties resulting from these properties, which create significant challenges for the design of an optimal filtering algorithm for this model. The main contributions of the article are outlined in the following section.

1.3. Optimal filtering for LWR PDE

Structural properties of the LWR PDE and its discretized forms impact the optimality of estimates produced by classical sequential estimation techniques. The main contributions of this article are the analysis and quantification of the lack of estimate optimality resulting from the following properties of the LWR PDE, and its numerical discretization using the Godunov scheme:

Nonlinearity of the fundamental diagram

One of the main properties of the LWR PDE is the nonlinearity of its flux function (fundamental diagram), which allows the modeling of traffic phases of different nature: *free-flow* and *congestion*. Nonlinearities of the model are the cause of the appearance of discontinuities in the solution of the partial differential equation. Consequently, the distribution of the uncertainty on the true state is a mixture distribution at shock waves even for unimodal noise distributions on the initial condition. In this article, we analytically show the emergence of mixture distributions in the solution of the PDE and numerically illustrate their importance on benchmark tests.

The mixture nature of the distribution of the uncertainty on the true state resulting from initial condition uncertainty propagating through an uncertain model raises the question of the relevance of minimal variance estimate for traffic applications. The estimate produced by classical filters may indeed correspond to a state with zero true probability, and the estimate covariance may exhibit large values corresponding to a variability due to the coexistence of different modes in the distribution of the uncertainty on the true state, each with significantly smaller covariance.

Non-differentiability of the discretized model

The most common numerical scheme used to compute the solution of the LWR PDE is the *Godunov scheme* [34], a finite volume scheme which consists of iteratively solving *Riemann problems* [35] between neighboring discretization cells and averaging their solution at each time-step on each spatial cell. In this article we prove that this scheme is non-differentiable and derive the expression of its non-differentiability domain.

The lack of differentiability of the Godunov scheme, a common discretization of the LWR PDE, is relevant for data assimilation algorithms whose optimality guarantees are based on Taylor series analysis, which assumes exact computation of the derivative up to a certain order. This is the case in particular for the EKF, which considers propagation of the estimate covariance using the tangent (linearized) model. Numerical results quantify estimate errors induced by this property of the discretized model. The result also affects the known order of accuracy of the estimate moments of the UKF, since in this case the Taylor series does not exist up to the required order.

This article can thus be viewed as a theoretical and numerical study of the implications of the structural properties of the Godunov scheme and CTM on filtering algorithms. It sheds some new light on the proper use of these schemes for traffic estimation purposes, and provides conclusions which are illustrated by detailed numerical studies.

While the results presented in this article are derived for the Godunov scheme, because historically is was one of the first numerical schemes proposed to solve scalar hyperbolic conservation laws (and the LWR PDE in particular), other proposed schemes such as the CTM exhibit the same features as the Godunov scheme, and thus our analysis applies to them as well.

The remainder of the article is organized as follows. Section 2 introduces the general theory of sequential data assimilation and optimal filtering. In Section 3 we present the most classical discrete and continuous macroscopic traffic models for which the study is conducted. Section 4 focuses on the *Riemann problem* which is the keystone of numerical solutions of continuous and discrete scalar conservation models and the focus of our subsequent analysis. Sections 5 and 6 point at the structural properties of macroscopic traffic models derived from the LWR PDE, in particular model nonlinearity in Section 5 and model non-differentiability in Section 6. Section 7 gives concluding remarks and examines associated issues regarding *data fusion*.

2. Sequential data assimilation

The theory of inverse problems [2] is concerned with the estimation of model parameters. A specific type of *inverse methods* consists in iteratively updating the estimates as data becomes available [36], instead of solving an inverse problem once using all measurements in batch. These so-called *sequential estimation algorithms*, particularly appropriate for on-line estimation, often rely on *Bayes' rule* and a computationally explicit optimality criterion (e.g. the *Gauss–Markov* theorem for *minimum mean squared error* (MMSE) estimation). In the case of additive noise, one of the most well-known sequential estimation algorithms is the seminal *Kalman filter* [5].

2.1. Kalman filter

Given a system with true state at time t denoted by Ψ_t, and Y_t the vector of all available observations up to time t, the *filtering problem* is concerned with the computation of an *optimal estimate* of Ψ_t for a predefined loss function. Solvability of the estimation problem heavily depends on the loss function used, and on the statistics considered.

The use of the *quadratic loss function* dates back to the estimation problem posed by Gauss in the 18th century for astronomy [37,38]. The solution proposed by Gauss is the so-called *least-squares method*, justified by the *Gauss–Markov* theorem [39]. The theorem proves that, assuming a linear observation model with additive white noise, the *best linear unbiased estimator* (BLUE) (best in the minimum variance sense), of a random process ψ_t can be computed as the solution to the *ordinary least squares* (OLS) problem.

The role of the quadratic norm for estimation is further emphasized by a result from Sherman [40], which shows that for a large class of loss functions, which includes the quadratic loss function, the mean of the conditional distribution $p(\psi_t|Y_t)$ is optimal.

Formally, given a loss function $L(\cdot)$ such that:

$$\begin{aligned} &L(0) = 0 \\ &\exists f \text{ real-valued convex s.t. } \quad \forall \psi_1, \psi_2 \quad \text{s.t.} \quad f(\psi_1) \geq f(\psi_2) \\ &\text{then} \quad L(\psi_1) \geq L(\psi_2), \end{aligned} \tag{1}$$

given a random variable ψ, if the probability density function associated with the random variable ψ is symmetric around the mean, and unimodal, then $\mathbb{E}(\psi)$ is the optimal estimator of ψ for the loss function $L(\cdot)$.

When applied to the conditional random variable $\psi_t|Y_t$, this shows that the conditional mean is the optimal estimator in the sense of the loss function $L(\cdot)$ for this particular class of loss functions and probabilities.

The statistical assumptions on the processes ψ_t and Y_t are tied to prior knowledge of the generative distributions. However, a significant computational argument in favor of the use of normal statistics is the optimality guarantee provided by combining the two arguments above. Without any assumption on the statistics, the Gauss–Markov theorem states that the BLUE is given by the solution to the OLS algorithm. Sherman's result (1) states that the solution of the OLS is the conditional mean. In the Gaussian case the conditional mean is linear, hence it is also the solution of the OLS with constraint that the estimator be linear. Hence the BLUE of the process is optimal, without restriction of linearity on the estimator, if we assume that the statistics are Gaussian.

In his seminal paper [5], Kalman provides a *sequential* algorithm to compute the BLUE of the state for *dynamical systems*, under additive white Gaussian noise, with a deterministic linear observation equation (this result was later extended to include additive white Gaussian observation noise). The KF is defined in a *state-space model*, which consists of a state equation and an observation equation. In the following, we denote by x_t the *state* at time t, a discrete computable approximation of the deterministic true state Ψ_t.

For transportation applications involving macroscopic variables, the state is typically a set of densities, speeds, or counts, defined on a discretization grid. The true state consists of the true traffic conditions on the road, which are only available to an oracle, or some high fidelity datasets such as the NGSIM dataset [41]. For simulation purposes, it is common practice to use a well-calibrated model, or a Monte Carlo simulation with high number of samples, as a proxy for the true state (to avoid the so-called *inverse crime* [2], the model used for estimation should be different from the model used for computing the true state).

We consider the following discrete linear model:

$$x_t = A_t\, x_{t-1} + w_t \tag{2}$$

where we denote by A_t the state model or time-varying state transition matrix at time t, and where the random variable $w_t \sim \mathcal{N}(0, W_t)$ is a white noise vector which accounts for modeling errors. In particular in this setting the true state Ψ_t is assumed to follow the dynamics A_t without additional noise. Measurements are modeled by the linear observation equation:

$$y_t = C_t\, \Psi_t + v_t \tag{3}$$

where $v_t \sim \mathcal{N}(0, V_t)$ is a white noise vector which accounts for measurement errors assumed uncorrelated with modeling errors, and C_t is the modeled measurement matrix at time t (also time-varying, to integrate the possibility of moving or intermittent sensors). The KF sequentially computes the BLUE at time $t+1$ from the BLUE at time t as follows:

$$\text{Forecast: } \begin{cases} x_{t+1|t} = A_{t+1}\, x_{t|t} \\ \Sigma_{t+1|t} = A_{t+1}\, \Sigma_{t|t}\, A_{t+1}^T + W_{t+1} \end{cases} \tag{4}$$

$$\text{Analysis: } \begin{cases} x_{t+1|t+1} = x_{t+1|t} + K_{t+1}\left(y_{t+1} - C_{t+1}\, x_{t+1|t}\right) \\ \Sigma_{t+1|t+1} = \Sigma_{t+1|t} - K_{t+1}\, C_{t+1}\, \Sigma_{t+1|t} \\ \text{where} \quad K_{t+1} = \Sigma_{t+1|t}\, C_{t+1}^T \left(C_{t+1}\, \Sigma_{t+1|t}\, C_{t+1}^T + V_{t+1}\right)^{-1}. \end{cases} \tag{5}$$

The forecast step (4) consists in propagating the mean and covariance of the state through the linear model (2). The analysis step (5) amounts to the computation of the conditional mean of the state given the observations, for the linear observation model (3) and jointly Gaussian statistics. The conditional covariance is computed similarly. From a Bayesian perspective, the Kalman filter

sequentially computes the posterior distribution of the state, based on the prior distribution given by the state-space model.

When the state model is not linear, there is no general analytical expression for the propagation of the statistics. Suboptimal filters of different types have been derived. *Stochastic* methods consider propagating the state through the nonlinear model using a sample representation. *Deterministic methods* consist in propagating analytical approximations of low order moments through the model. Stochastic methods require in general sampling schemes and pseudo-random generators for the correct execution of the filters, unlike deterministic methods.

2.2. Deterministic filters

In this section we present the EKF and the UKF for nonlinear systems. The EKF forecast step is based on model linearization. The UKF consists in representing exactly the first two moments of the prior distribution by a set of deterministic samples. In particular, no sampling term is required for the application of these algorithms.

2.2.1. Extended Kalman filter

The EKF is an extension of the KF for nonlinear state-space models. The EKF consists in using a Taylor series truncation of the model at the current state to propagate the state statistics. We present the case of a nonlinear state model combined with a linear observation model, although a nonlinear observation equation can also be considered through a similar linearization of the observation operator at the analysis step. The forecast mean is given by the nonlinear model, whereas the forecast covariance is given by a first order approximation of the model. If we denote by A_{t+1} the linearization of the nonlinear model dynamics $\mathcal{A}(\cdot, t)$ at the state estimate $x_{t|t}$, the forecast and analysis steps for the EKF read:

$$\text{Forecast: } \begin{cases} x_{t+1|t} = \mathcal{A}(x_{t|t}, t) \\ \Sigma_{t+1|t} = A_{t+1}\, \Sigma_{t|t}\, A_{t+1}^T + W_{t+1} \end{cases} \tag{6}$$

$$\text{Analysis: } \begin{cases} x_{t+1|t+1} = x_{t+1|t} + K_{t+1}\left(y_{t+1} - C_{t+1}\, x_{t+1|t}\right) \\ \Sigma_{t+1|t+1} = \Sigma_{t+1|t} - K_{t+1}\, C_{t+1}\, \Sigma_{t+1|t} \\ \text{where} \quad K_{t+1} = \Sigma_{t+1|t}\, C_{t+1}^T \left(C_{t+1}\, \Sigma_{t+1|t}\, C_{t+1}^T + V_{t+1}\right)^{-1} \end{cases} \tag{7}$$

where the only difference from the Kalman filter resides in the propagation of the state mean at the forecast step, using the nonlinear state model. Different sources of sub-optimality arise in the derivation of the EKF:

1. *Accuracy of the Taylor truncation*:
   a The model approximation used at the forecast step (6) for the covariance propagation requires that the model Jacobian be accurately computed.
   b The mean given by the EKF is a first order Taylor series approximation of the MMSE, whereas the covariance is a third order approximation of the MMSE covariance.
2. *Closure assumption*: it is assumed that there is no significant interaction between higher order statistics and the first two moments of the state estimate.

Cases in which the closure assumption breaks, due to the importance of higher order terms in the model Taylor series have been documented, with illustrations of estimates biased and inconsistent [12], and with diverging error statistics [42]. Cases in which this assumption breaks, due to the importance of higher-order statistics can be found in [43,44] in the case of bimodal distributions.

Remark 1. An approximation made in the EKF equations lies in the propagation of the state covariance $\Sigma_{t+1|t}$. This covariance is then used at the analysis step (7) at which observations are combined with the model forecast. The study of the resulting error structure of the state covariance after propagation in the context of traffic is to the best of our knowledge an open problem, and is a focus of this article.

2.2.2. Unscented Kalman filter

The UKF [12] is built on the unscented transformation, which consists in representing a distribution with mean μ and variance Σ by a set of weighted samples, or *sigma points*, chosen deterministically such that the weighted sample mean is μ and the weighted sample covariance is Σ [45]. For a state-space of dimension n, the $2n+1$ sigma points produced by the unscented transformation are defined as

$$\begin{cases} x^0 = \mu \\ x^k = \mu + \left((n+\kappa)\,\Sigma\right)_k^{\frac{1}{2}} \quad k = 1, \ldots, n \\ x^{k+n} = \mu - \left((n+\kappa)\,\Sigma\right)_k^{\frac{1}{2}} \quad k = 1, \ldots, n \end{cases} \tag{8}$$

where $\left((n+\kappa)\,\Sigma\right)_k^{1/2}$ denotes the kth column of the square root of $(n+\kappa)\,\Sigma$. The corresponding weights w^k are parameterized by κ, which controls the spread of the sigma points:

$$\begin{cases} w^0 = \dfrac{\kappa}{\kappa + n} \\ w^k = \dfrac{1}{2(\kappa+n)} \quad k = 1, \ldots, n \\ w^{k+n} = \dfrac{1}{2(\kappa+n)} \quad k = 1, \ldots, n. \end{cases} \tag{9}$$

Choosing the samples according to (8) and the weights according to (9) yields that the weighted sample mean and weighted sample covariance are equal to the distribution mean and covariance for any choice of κ. The forecast and analysis step of the augmented UKF [46] can be written as:

$$\text{Forecast: } \begin{cases} \text{Propagate sigma-points} \\ \quad x_{t+1|t}^k = \mathcal{A}(x_{t|t}^k, t) \quad k = 0, \ldots, 2n \\ \text{Compute forecast mean and covariance} \\ \quad x_{t+1|t} = \displaystyle\sum_{k=0}^{2n} w_k\, x_{t+1|t}^k \\ \quad \Sigma_{t+1|t} = \displaystyle\sum_{k=0}^{2n} w_k \left(x_{t+1|t}^k - x_{t+1|t}\right)\left(x_{t+1|t}^k - x_{t+1|t}\right)^T \end{cases} \tag{10}$$

Analysis:

$$\begin{cases} \text{Compute sigma-points observations} \\ \quad z_{t+1|t}^k = \mathcal{C}_{t+1}\, x_{t+1|t}^k \quad k = 0, \ldots, 2n \\ \text{Compute observation mean and covariance} \\ \quad z_{t+1|t} = \displaystyle\sum_{k=0}^{2n} w_k\, z_{t+1|t}^k \\ \quad Z_{t+1|t} = \displaystyle\sum_{k=0}^{2n} w_k \left(z_{t+1|t}^k - z_{t+1|t}\right)\left(z_{t+1|t}^k - z_{t+1|t}\right)^T \\ \text{Compute covariance between forecast and observation} \\ \quad Y_{t+1|t} = \displaystyle\sum_{k=0}^{2n} w_k \left(x_{t+1|t}^k - x_{t+1|t}\right)\left(z_{t+1|t}^k - z_{t+1|t}\right)^T \\ \text{Compute posterior mean and covariance} \\ \quad x_{t+1|t+1} = x_{t+1|t} + K_{t+1}\left(y_{t+1} - z_{t+1|t}\right) \\ \quad \Sigma_{t+1|t+1} = \Sigma_{t+1|t} - K_{t+1}\, Z_{t+1|t}\, K_{t+1}^T \\ \quad \text{where} \quad K_{t+1} = Y_{t+1|t}\, Z_{t+1|t}^{-1} \end{cases} \tag{11}$$

where the unscented transformation is first used to compute the sigma points for the current estimates, which are then propagated through the model and whose mean and covariance is computed (10). At the analysis step, the forecast observation associated

with each sigma point through the (potentially) nonlinear observation model $\mathcal{C}_{t+1}$, is computed as $z^k_{t+1|t}$, which allows the computation of the observation mean $z_{t+1|t}$, observation covariance $Z_{t+1|t}$, and the covariance between forecast state and observation as $Y_{t+1|t}$. The analysis mean and covariance are then computed exactly using Kalman equations (11).

Different sources of sub-optimality arise in the UKF:

1. *Limited number of samples*: the mean and the covariance propagated by the UKF are third order approximations of the MMSE and MMSE covariance.
2. *Closure assumption*: it is assumed that there is no significant interaction between higher order statistics and the first two moments of the state estimate.

The UKF has been applied to traffic estimation [31] and was compared with the EKF for the Papageorgiou model (23). The two filters were empirically shown to have similar performances for joint state and parameter estimation [46] for this model (23). The results of this comparison are completed by the analysis presented in the present article in Sections 5 and 6, in which we study the state distribution features due to model nonlinearities and non-differentiability analytically and numerically in the case of the LWR model, and in which we show how they affect the EKF and the UKF. In particular we analyze the true distribution structure at shock waves of the LWR model, in the continuous and discrete domain. The Papageorgiou model is defined in the discrete domain, and exhibits an anticipation term which reduces the sharpness and amplitude of spatial variations. Consequently, the impact of the existence of shock waves on the performance of the filters is stronger in the case of the LWR model in the continuous domain, as illustrated in the present article.

2.3. Stochastic filters

A wide variety of filters extend the Kalman filter for nonlinear state models by representing the state by a set of random samples (*particles*, *ensemble members*). The rules for sample propagation, update, and for resampling, are of different types. The need for pseudo-random generator at every step of these algorithms justifies the appellation *stochastic filters*.

2.3.1. Ensemble Kalman filter

The EnKF [47,13] consists in representing the state statistics by a set of ensemble members which are evolved in time and whose mean is an estimator of the true state. The state error covariance is represented by the ensemble covariance. Formally, with N ensemble members, the EnKF equations read:

Forecast:

$$\begin{cases} x^k_{t+1|t} = \mathcal{A}(x^k_{t|t}, t) + w^k_{t+1} \quad k = 1, \ldots, N \\ x_{t+1|t} = \dfrac{1}{N} \displaystyle\sum_{k=1}^{N} x^k_{t+1|t} \\ \Sigma_{t+1|t} = \dfrac{1}{N-1} \displaystyle\sum_{k=1}^{N} \left(x^k_{t+1|t} - x_{t+1|t}\right) \left(x^k_{t+1|t} - x_{t+1|t}\right)^T \end{cases} \tag{12}$$

Analysis:

$$\begin{cases} x^k_{t+1|t+1} = x^k_{t+1|t} + K_{t+1} \left(y_{t+1} + v^k_{t+1} - C_{t+1}\, x^k_{t+1|t}\right) \quad k = 1, \ldots, N \\ \Sigma_{t+1|t+1} = \Sigma_{t+1|t} - K_{t+1}\, C_{t+1}\, \Sigma_{t+1|t} \\ \text{where} \quad K_{t+1} = \Sigma_{t+1|t}\, C^T_{t+1} \left(C_{t+1}\, \Sigma_{t+1|t}\, C^T_{t+1} + V_{t+1}\right)^{-1}. \end{cases} \tag{13}$$

In the limit of large number of samples, the EnKF converges toward the KF for linear systems. Due to the independent ensemble forecasts (12), it is *embarrassingly parallel* and particularly appropriate for efficient distributed computations. At the analysis step (13), the modeled observation noise is explicitly added to the measured observation, to capture the full observation noise in the analysis equation [48]. In the context of traffic estimation, the EnKF has been applied to the Bay Area highway networks with a traffic model equivalent to the LWR PDE, formulated using a velocity variable [29]. The principal source of sub-optimality arising in the EnKF is sampling error:

1. *Sampling error*: the use of a finite number of ensemble members introduces a sampling error in the estimate distribution.

Remark 2. The covariance given by the EnKF is the state error covariance and not the state covariance. In the KF, the state mean and state error covariance are propagated analytically. The state error covariance coincides with the state covariance. On the other hand, the EnKF analytically propagates ensemble members whose mean is an unbiased estimator of the state mean, and covariance coincides by definition of the update equations with the state error covariance, but not with the state covariance, except in the limit of an infinite number of ensemble members.

Extensions of the EnKF allowing to obtain higher order moments of the state distribution have also been considered [49] by integrating a modified analysis step.

2.3.2. Particle filter

The PF, also known as *bootstrap filter*, or sequential Monte Carlo method [50,30,14] can be traced back to the seminal articles of Metropolis and Ulam [51], later generalized by Hastings [52]. These methods represent the full statistics of the state by a set of samples which are propagated through the state model. When observations are received, sample weights are scaled by the relative likelihood of the new observation, and the updated representation of the probability distribution is re-sampled. Formally, the PF steps in the case of N particles are as follows:

Forecast: $x^k_{t+1|t} = \mathcal{A}(x^k_{t|t}, t) + w^k_{t+1} \quad k = 1, \ldots, N$

Analysis:
$$\begin{cases} \text{Re-weighting:} \\ \quad \alpha^k_{t+1} = \alpha^k_t \dfrac{p(y_{t+1}|x^k_{t+1|t})}{\displaystyle\sum_{k=1}^{N} \alpha^k_t\, p(y_{t+1}|x^k_{t+1|t})} \quad k = 1, \ldots, N \\ \text{Re-sampling:} \\ \quad \text{Generate } N \text{ samples } x^k_{t+1|t+1} \\ \quad \text{from the distribution defined by} \\ \quad P(X = x^k_{t+1|t+1}) = \alpha^k_{t+1}, k = 1, \ldots, N. \end{cases}$$

The PF has been applied to the case of transportation systems [28] on the stochastic model described in [53]. The particle filter is the only filtering method able to capture the complete state distribution, in the limit of infinite number of samples, without restrictive assumption on the dynamics or on the statistics. Well-known weaknesses of the PF relate to the problem of sample degeneracy for high dimensional [54] systems. The use of an appropriate *proposal distribution* at the re-weighting step is key to reducing the sample weight variance given the system history, but more sophisticated *importance sampling* or *rejection sampling* techniques are often considered [50,55]. The sources of sub-optimality in the PF relate to:

1. *Sampling error:* the use of a finite number of particles introduces a sampling error in the estimate distribution.

The *implicit particle filter* is a notable extension [56] of the PF which allows a priori the definition of the desired weights of the particles after analysis and thus alleviation of the problem of sample degeneracy in the case of the *exponential family*. Another research track has explored the use of the EKF, EnKF or UKF to compute a proposal distribution in the particle filter [55].

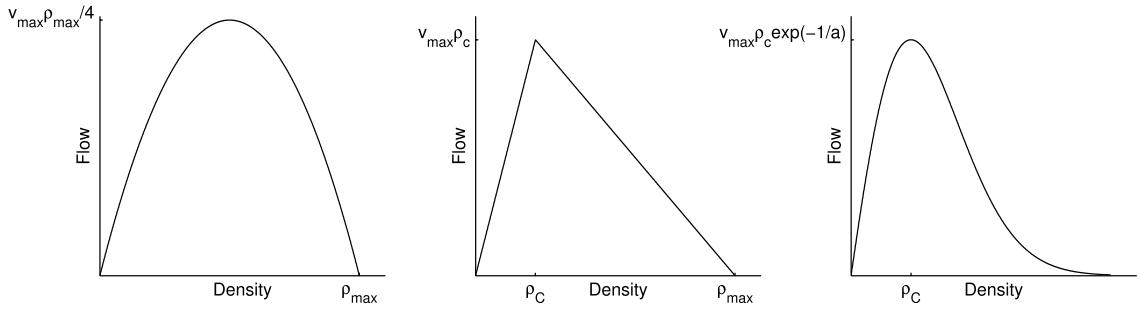

Fig. 1. *Fundamental diagrams:* Greenshields (left), triangular (center), exponential (right).

Sustained improvements of the filters presented above have been in large part driven by specific improvements for systems exhibiting strong nonlinearity or non-normality, identified as the causes of inaccurate estimates and forecast. In the following section, we present the seminal macroscopic traffic models which have been considered for real-time data assimilation on transportation networks. The subsequent sections will then focus on the analysis of the performance of the respective filtering schemes on the models, which is one of the contributions of the article.

3. Macroscopic traffic modeling

Macroscopic traffic modeling consists of considering traffic phenomena as a continuum of vehicles, instead of modeling individual vehicle dynamics. Macroscopic traffic models are historically inspired from constitutive hydrodynamics models, which exhibit similar properties to traffic flow. In this section we introduce one of the most common scalar traffic models, as well as some non-scalar models classically used for estimation.

3.1. Scalar models of traffic flow

Classical scalar models of traffic consider the traffic state at a point x at time t to be fully represented by the density $\rho(t, x)$ of vehicles at this point. The evolution of the density of vehicles can be modeled by a combination of physical principles, statistical properties, and empirical findings. All the models considered in this section are single-lane single-class models of traffic.

3.1.1. Continuous models

A classical state equation used to model the evolution of the density $\rho(\cdot, \cdot)$ of vehicles on the road network is the LWR PDE [32,33], which expresses the conservation of vehicles on road links:

$$\partial_t \rho + \partial_x Q(\rho) = 0 \tag{14}$$

where the flux function $Q(\cdot)$, assumed to be space–time invariant on limited space–time domains, denotes the realized flux of vehicles with the density ρ, at the stationary state. The flux function, or *fundamental diagram*, is classically given by an empirical fit of the relation between density and flow. It can be equivalently given by an empirical fit $V(\cdot)$ of the relation between density and space-mean speed, which allows us to define the flux function as:

$$Q(\rho) = q = \rho\, v = \rho\, V(\rho),$$

where the central equality is a definition of the flow q. A variety of parametric flux functions can be found in the literature. One of the earliest flux functions is the *Greenshields flux function* [57] or quadratic flux function (represented in Fig. 1, left), which expresses a linear relationship between density and speed, or equivalently a quadratic relation between density and flow:

$$Q(\rho) = v_{\max}\, \rho \left(1 - \frac{\rho}{\rho_{\max}}\right) \tag{15}$$

where $v_{\max}$ denotes the *free-flow speed* and $\rho_{\max}$ the *jam density*. The *Newell–Daganzo flux function* [27,58] or triangular flux function, represented in Fig. 1, center, is a piecewise linear function of the density, with different slopes in free-flow and congestion:

$$Q(\rho) = \begin{cases} \rho\, v_{\max} & \text{if } \rho \in [0, \rho_c] \\ \rho_c\, v_{\max} \dfrac{\rho_{\max} - \rho}{\rho_{\max} - \rho_c} & \text{if } \rho \in [\rho_c, \rho_{\max}] \end{cases} \tag{16}$$

where ρ_c denotes the critical density, which represents the density at which the realized flow is maximal. The speed of backward moving waves in congestion is given by $w = v_{\max}\, \rho_c/(\rho_c - \rho_{\max})$. Variations on a flux function based on an exponential relation between density and flow [59,20], parameterized by a, such as the one represented in Fig. 1, right, can be found in the literature:

$$Q(\rho) = \rho\, v_{\max} \exp\left(-\frac{1}{a}\left(\frac{\rho}{\rho_c}\right)^a\right). \tag{17}$$

The interested reader might also consider the *Greenberg* fundamental diagram [60] or the *Van-Aerde* fundamental diagram [61].

Remark 3. The LWR PDE models the evolution of traffic flow on a road segment with uniform topology. A junction is defined by a change of topology (crossing, number of lanes, speed limit, curvature, etc.) on a road segment, which requires specific efforts for physical consistency and mathematical compatibility with the link model. A junction can be modeled as a vertex of the graph representing the road network. With each vertex is associated an allocation matrix A, where a_{ij} expresses the proportion of the incoming flow from link j going to link i. For uniqueness of the solution of the junction problem, different conditions have been considered in the literature: for instance maximizing the incoming flow through the junction [62,27] or maximizing a concave function of the incoming flow [63]. A formulation using internal dynamics for the junction [64] has been shown to be equivalent to the vertex models for the merge and diverge junction. The interested reader is referred to the book by Garavello and Piccoli [65] for more details on the junction problem.

For traffic applications, given an initial condition $\rho_0(\cdot)$ defined on a stretch $[0, L]$, using the LWR model requires solving the associated *Cauchy problem*, defined as the problem of existence and uniqueness of a solution to the LWR PDE with initial condition $\rho_0(\cdot)$. If the initial condition is piecewise constant (which is the case for many numerical approximations) and self-similar,[1] the Cauchy problem reduces to the Riemann problem

[1] A function f of n variables $x_1, \ldots, x_n$ is called self-similar if $\forall \alpha > 0 \in \mathbb{R}, f(\alpha x_1, \ldots, \alpha x_n) = f(x_1, \ldots, x_n)$.

(see Section 4.2). We focus our analysis for data assimilation on the Riemann problem, which, by its simplicity, allows full analytical and numerical characterization of the relation between initial condition uncertainty and structure of the uncertainty in the solution to the PDE.

3.1.2. Discretized link models

Given a discretization grid defined by a space-step Δx and a time-step Δt, if we denote by ρ_i^n the discretized solution at $i\,\Delta x$, $n\,\Delta t$ and $\mathcal{C}_i^n$ the cell defined by $\mathcal{C}_i^n = [n\,\Delta t, (n+1)\,\Delta t] \times [i\,\Delta x, (i+1)\,\Delta x]$, the discretization of the LWR PDE using the *Godunov scheme* [34] reads:

$$\rho_i^{n+1} = \rho_i^n + \frac{\Delta t}{\Delta x}\left(q_G(\rho_{i-1}^n, \rho_i^n) - q_G(\rho_i^n, \rho_{i+1}^n)\right) \tag{18}$$

where the numerical Godunov flux $q_G(\cdot,\cdot)$ is defined as follows for a concave flux function $Q(\cdot)$ with a maximum at ρ_c:

$$q_G(\rho_l, \rho_r) = \begin{cases} Q(\rho_l) & \text{if } \rho_r \le \rho_l < \rho_c \\ Q(\rho_c) & \text{if } \rho_r \le \rho_c \le \rho_l \\ Q(\rho_r) & \text{if } \rho_c < \rho_r \le \rho_l \\ \min(Q(\rho_l), Q(\rho_r)) & \text{if } \rho_l < \rho_r. \end{cases} \tag{19}$$

Remark 4. Another common scheme for hyperbolic conservation laws is the *random approximation scheme* introduced by Glimm [66], which consists in constructing an approximate solution by randomly sampling from the values of the solution in a neighborhood at the previous time step. For the sake of concision, the analysis in the present article is limited to finite volume methods, and the Godunov scheme in particular.

The Godunov scheme is a first order finite volume discretization scheme commonly used for numerical computation of *weak entropy solutions* to one-dimensional conservations laws such as the LWR PDE [67]. The design of the Godunov scheme dynamics (18) results from the following steps:

1. At time $n\,\Delta t$, for each couple of neighboring cells $\mathcal{C}_i^n$, $\mathcal{C}_{i+1}^n$, compute the solution to the Riemann problem defined at the intersection of cells $\mathcal{C}_i^n$, $\mathcal{C}_{i+1}^n$, by the left datum ρ_i^n and the right datum ρ_{i+1}^n.
2. At time $(n+1)\,\Delta t$, on each domain $\{(n+1)\,\Delta t\} \times [i\,\Delta x, (i+1)\,\Delta x]$ compute the average of the solution of the Riemann problem. Specifically, integrating the LWR PDE on the domain $\mathcal{C}_i^n$,

$$\iint_{\mathcal{C}_i^n}\left(\frac{\partial \rho}{\partial t} + \frac{\partial Q(\rho)}{\partial x}\right) ds dy = 0 \tag{20}$$

and applying the Stokes theorem on $\mathcal{C}_i^n$ to this equality yields:

$$\Delta x\,\rho_i^{n+1} - \int_{n\,\Delta t}^{(n+1)\,\Delta t} Q(\rho(s, i\,\Delta x))ds - \Delta x\,\rho_i^n + \int_{n\,\Delta t}^{(n+1)\,\Delta t} Q(\rho(s, (i+1)\,\Delta x))ds = 0, \tag{21}$$

where we denote by ρ_i^{n+1} the space average of the solution to the Riemann problems on $\{(n+1)\,\Delta t\} \times [i\,\Delta x, (i+1)\,\Delta x]$. Since the solution to the Riemann problems is auto-similar, hence constant at $i\,\Delta x$ and $(i+1)\,\Delta x$, if we denote respectively by $Q(\rho_{i-1}^n, \rho_i^n)$, $Q(\rho_i^n, \rho_{i+1}^n)$ the values of the corresponding flow at these locations over the interval $[n\Delta t, (n+1)\,\Delta t]$, we obtain:

$$\Delta x\,\rho_i^{n+1} - \Delta x\,\rho_i^n = \Delta t\,Q(\rho_{i-1}^n, \rho_i^n) - \Delta t\,Q(\rho_i^n, \rho_{i+1}^n),$$

which is the dynamics equation (18) of the Godunov scheme.

The first step of the Godunov scheme is exact whereas the second step, through averaging, introduces numerical diffusion (see [67] for more details). The consequence of this diffusion on estimation is further discussed in Section 5.

Remark 5. It must be noted that grid-free algorithms allow us to compute numerical solutions of scalar conservation laws without numerical diffusion [68], with a higher complexity in general. In the case of transportation, some algorithms have been shown to be exact for specific fundamental diagrams and particular initial and boundary conditions [69–72].

The Godunov scheme has been shown to provide a numerical solution consistent with classical traffic assumptions [73] and to be equivalent to the *supply–demand* formulation for concave flux functions with a single maximum. In the case of a triangular flux function (16), the Godunov scheme reduces to the CTM [26,27]:

$$q_G(\rho_l, \rho_r) = \min\left(\rho_l V, \rho_c V, \rho_c V \frac{\rho_{\max} - \rho_r}{\rho_{\max} - \rho_c}\right),$$

which thus inherits the properties causing the filtering difficulties motivating the present article. The Godunov scheme (18) defines the state equation used by the estimation algorithms from Section 2. Analysis of the nonlinearity and non-differentiability of the Godunov scheme in the context of estimation are the subject of Sections 5.2 and 6.

3.2. Non-scalar models of traffic flow

Non-scalar models of traffic flow consider additional state variables and additional physical principles to model traffic states. One of the first non-scalar traffic flow models is the *Payne–Whitham* model [74,75]:

$$\begin{cases} \partial_t \rho + \partial_x q = 0 \\ \partial_t v + v\,v_x + \dfrac{c_0^2}{\rho}\,\partial_x \rho = \dfrac{V(\rho) - v}{\tau}. \end{cases} \tag{22}$$

The first equation expresses the conservation of vehicles, and the second equation models the evolution of speed, which is subject to convection, anticipation, and relaxation (respectively second and third left-hand side terms of second equation, and right-hand side term of the second equation).

The EKF has been applied to networks[2] for state and parameter estimation [18,19], with the following discretization of the *Payne–Whitham* model Eq. (22):

$$\begin{cases} \rho_i^{n+1} = \rho_i^n + \dfrac{\Delta t}{\Delta x}\left(q_{i-1}^n - q_i^n\right) \\ v_i^{n+1} = v_i^n + \dfrac{\Delta t}{\Delta x}\,v_i^n\left(v_{i-1}^n - v_i^n\right) + \dfrac{\Delta t}{\tau}\left(V(\rho_i^n) - v_i^n\right) \\ \qquad - \dfrac{c_0^2\,\Delta t}{\Delta x}\dfrac{\rho_{i+1}^n - \rho_i^n}{\rho_i^n + \kappa} \\ q_i^n = \rho_i^n\,v_i^n \end{cases} \tag{23}$$

where κ is a regularization parameter and the function $V(\cdot)$ is the exponential fundamental diagram (17). Other notable models with two state variables (so-called *second order models*) include the *Aw–Rascle* model [76], the *non-equilibrium* model [77], or the *phase transition* model [78,79]. Traffic models with three state variables have also been proposed [80] by addition of a state equation for the variance.

In this article, we focus our analysis on scalar models and specifically on nonlinearity and non-differentiability of the flow

[2] For simplicity we omit the network terms (sources and sinks) in equation (23).

associated with the Riemann problem, which is an example of a Cauchy problem representing the evolution of traffic discontinuities, which are critical for several applications (see following Section 4.1). This applies on a case-by-case basis to higher order models with similar features. The discrete second order model (23) is by definition unable to capture discontinuities exactly, and differentiable, however structural properties of the continuous Payne–Whitham model from which it is derived exhibit similarities with the LWR model [81] and allow the generalization of some of our conclusions.

4. Discontinuities and uncertainty

At the macroscopic level, traffic flow exhibits nonlinearities which can be modeled using nonlinear conservation laws such as the LWR PDE (14). Nonlinearities are the cause for discontinuities which may arise in finite time in the solution to the Cauchy problem associated with the PDE even with smooth initial and boundary data. According to the definition of the solution to the Riemann problem (25), shock waves persist when, at a spatial discontinuity, the upstream density is lower than the downstream density. Thus they cannot be neglected by any traffic application. Physically, these discontinuities model the existence of queues, which are one of the main foci of traffic flow research.

4.1. Estimation and control

Queue extremities are phenomena with very limited spatial extent, which characterize the interface between significantly different phases of traffic flow. This property makes them relatively hard to directly measure and monitor using classical fixed sensing infrastructure. This is especially true when the upstream end of the queue is stationary, and can only be directly measured if it lies on a fixed sensor or by probe vehicles reporting measurements exactly at the corresponding location.

Large traffic variations occurring on a short spatial extent, typical of queue extremities, make them particularly hazardous, and being able to alert drivers of sudden changes in speed is one of the focal points of traffic safety applications [82].

For control applications, accurately locating the location and propagation speed of queues is critical. Their location typically impacts ramp metering algorithms directly, since they are often designed around the values of the upstream and downstream flow at the upstream end of the queue. In the absence of sensors, the algorithm depends on the estimated flows upstream and downstream of the ramp.

Furthermore, accurate estimation of the propagation speed of queues is one of the most essential components of traffic forecast and dynamic travel-time estimation. Estimating their propagation speed requires the estimation of the left and right density at the queue extremities, as well as accurate knowledge of the fundamental diagram.

In the context of model-based estimation, the influence of model nonlinearity and non-differentiability on the quality of the estimates for traffic phenomena has not received much attention in the traffic community with a few notable exceptions [46,83] (see [84] for a related problem for atmospheric models, and [85] for a study of non-differentiability in a general context). In the following section, we consider the Riemann problem, which is a benchmark problem for studying the solution to the LWR PDE, and the evolution of shock waves. We then consider in Section 4.3 the Riemann problem with a stochastic datum, which is used in the following sections as a framework for the study of the propagation of discontinuities in the presence of uncertainties.

4.2. Riemann problem

The Riemann problem is a Cauchy problem with a self-similar initial condition, of the form:

$$\rho(t=0,x)=\begin{cases}\rho_l & \text{if } x<0\\ \rho_r & \text{if } x>0.\end{cases} \tag{24}$$

The solution to the Riemann problem is the solution to the Cauchy problem associated with the PDE with initial condition the Riemann datum (24). The Riemann problem is a key building block for proofs of existence of solutions to the Cauchy problem for general initial conditions in the space of *bounded variations* (BV), via Helly's theorem [68]. It is also critical to the design of numerical schemes such as the wavefront tracking method [68] and the Godunov scheme, which proceeds by iteratively solving the Riemann problem between discretization cells, before averaging its solution on each cell (see Eqs. (20) and (21)).

For a flux function $Q(\cdot)$ with constant concavity sign, the unique entropy solution to the Riemann problem is defined for $(t,x)\in\mathbb{R}^+\setminus\{0\}\times\mathbb{R}$ as follows

1. If $Q'(\rho_l)>Q'(\rho_r)$ the solution is a shock wave

$$\rho_R\left(\frac{x}{t},\rho_l,\rho_r\right)=\begin{cases}\rho_l & \text{for } \dfrac{x}{t}<\sigma\\ \rho_r & \text{for } \dfrac{x}{t}>\sigma\end{cases} \tag{25}$$

   where the location of the discontinuity is $x=\sigma t$, with σ given by the Rankine–Hugoniot relation:

$$\sigma=\frac{Q(\rho_l)-Q(\rho_r)}{\rho_l-\rho_r} \tag{26}$$

   which expresses the conservation of ρ at the discontinuity.
2. If $Q'(\rho_l)<Q'(\rho_r)$ the solution is a rarefaction wave

$$\rho_R\left(\frac{x}{t},\rho_l,\rho_r\right)=\begin{cases}\rho_l & \text{for } \dfrac{x}{t}\le Q'(\rho_l)\\ (Q')^{-1}\left(\dfrac{x}{t}\right) & \text{for} \dfrac{x}{t}\in(Q'(\rho_l),Q'(\rho_r))\\ \rho_r & \text{for } \dfrac{x}{t}\ge Q'(\rho_r).\end{cases}$$

The interested reader is referred to Evans [35] and Leveque [67] for more details, and Garavello and Piccoli [65] in the context of traffic. Shock waves and rarefaction waves respectively model the upstream and downstream ends of a queue. One may note that depending on the flow difference at the discontinuity, the propagation speed may be positive or negative.

Remark 6. This brief description of the Riemann problem for the scalar conservation law is also of interest for continuous non-scalar traffic models in which discontinuities arise (see [78,81]).

For estimation purposes, it is appropriate to consider the uncertain Riemann datum, which requires the definition of the Riemann problem with stochastic datum.

4.3. Riemann problem with stochastic datum

We consider a Riemann problem for the PDE (14) with stochastic datum [86] defined by:

$$\rho(t=0,x)=\begin{cases}\varrho_l & \text{if } x<0\\ \varrho_r & \text{if } x>0\end{cases} \tag{27}$$

where ϱ_l,ϱ_r are random variables. We further denote by ς the random variable defining the resulting shock speed, whose distribution is given by the distribution of the Rankine–Hugoniot

speed (26) for the realizations of the stochastic datum (ϱ_l, ϱ_r). We focus our analysis on the case in which each realization of the solution to the Riemann problem with stochastic datum is a shock wave. In the following proposition, we derive the analytical expression of the random field solution of the Riemann problem with stochastic datum in this case.

Proposition 1. *The solution of the Riemann problem with stochastic datum* (ϱ_l, ϱ_r) (27) *with bounded support, respectively* $\mathcal{D}_l$, $\mathcal{D}_r$ *such that* $\sup(\mathcal{D}_l) < \inf(\mathcal{D}_r)$*, is a random field* $\varrho_{t,x}$*, defined by:*

$$P\left(\varrho_{t,x} = \rho\right) = P\left(\varrho_l = \rho | \varsigma > \frac{x}{t}\right) P\left(\varsigma > \frac{x}{t}\right) + P\left(\varrho_r = \rho | \varsigma < \frac{x}{t}\right) P\left(\varsigma < \frac{x}{t}\right). \tag{28}$$

Proof. By assumption on the Riemann datum, $\sup(\mathcal{D}_l) < \inf(\mathcal{D}_r)$, the solution of a realization of the Riemann problem is a shock wave between a realization ρ_l of ϱ_l and a realization ρ_r of ϱ_r, with shock-wave speed given by the Rankine–Hugoniot relation (26) which defines the realizations of the stochastic shock-wave speed ς. If we denote by $\mathbf{1}_I$ the characteristic function of interval I, the solution to a realization of the Riemann problem at $(t, x) \in \mathbb{R}^+ \setminus \{0\} \times \mathbb{R}$ is given by:

$$\rho = \rho_l \mathbf{1}_{\sigma > \frac{x}{t}} + \rho_r \mathbf{1}_{\sigma < \frac{x}{t}}$$

which is the solution of the deterministic Riemann problem in the case of a shock wave (25). For $(t, x) \in \mathbb{R}^+ \setminus \{0\} \times \mathbb{R}$, a realization σ of the shock-wave speed such that $\sigma > x/t$, the solution is drawn from the left datum, which reads:

$$P\left(\varrho_{t,x} = \rho | \varsigma > \frac{x}{t}\right) = P\left(\varrho_l = \rho | \varsigma > \frac{x}{t}\right).$$

Writing the similar equation for the case $\sigma < \frac{x}{t}$ and using the law of total probability, we obtain equality (28), and the proof. □

The case in which the supports of the left and right data do not intersect and are such that all realizations of the Riemann problem are rarefaction waves can be treated similarly. For simplicity, we do not address here the case where the supports of the left and right data have a non-empty intersection and consequently the realization of the solution to the Riemann problem can be a shock wave or a rarefaction wave.

Remark 7. For numerical simulations, correlated initial noise in the Godunov scheme accurately models the Riemann problem. Specifically, the Riemann problem with stochastic datum can be modeled numerically by using the same realization of left initial noise for all cells on the left of the discontinuity in the discrete initial condition, and the same realization of the right initial noise for all cells on the right of the discontinuity in the discrete initial condition.

In the two following sections, we consider a Riemann problem with stochastic datum modeling initial condition error. We show specific consequences of the nonlinearity of the PDE on the statistics of the distribution of the uncertainty on the true state and compare the true solution of the so-called *stochastic Riemann problem* with forecast state estimates given by the EKF, UKF and EnKF. We also consider the solution to the discrete Godunov scheme and assess how diffusion and modeling errors impact the applicability of the conclusions drawn for the continuous solution to the discrete solution.

5. Model nonlinearity

In this section, we present the consequences of model nonlinearities on the estimate statistics propagated by different schemes. We show that propagating only the first two moments of the distribution can lead to significant estimation error at shock waves where mixture distributions between the left and right state arise and propagate. We show that despite modeling error and numerical diffusion, this phenomenon is also present in the solution to the Godunov scheme. We focus our analysis on the EKF, EnKF and UKF, which offer distinct properties; the EKF consists in a linearization of the model, the EnKF exhibits stochastic error and converges toward the classical Kalman filter in the limit of infinite number of samples, and the UKF consists in deterministic sampling toward accurate propagation of the first two moments of the estimate distribution.

5.1. Mixture solution to the Riemann problem

In this section we show that the existence of discontinuities in the solution to the PDE combined with the existence of stochastic terms in the state-space model may introduce mixture distributions that travel with shock waves and propagate around them.

We denote by $\mathcal{D}$ the set of points (t, x) for which there is a non-zero probability that, in the (x, t) plane, a realization of the solution to the Riemann problem with stochastic datum (27) exhibits a discontinuity on the left of (t, x) and a non-zero probability that a realization exhibits a discontinuity on the right of (t, x):

$$\mathcal{D} = \left\{(t, x) \in \mathbb{R}^+ \setminus \{0\} \times \mathbb{R} | \min\{P(\varsigma < x/t), P(\varsigma > x/t)\} > 0\right\}.$$

Proposition 2. *In the domain* $\mathcal{D}$*, the solution to the Riemann problem with stochastic datum* (27) *is a mixture distribution.*

Proof. Outside of $\mathcal{D}$, we have by definition $P(\varsigma < x/t) = 0$ or $P(\varsigma > x/t) = 0$. According to Eq. (28), in the first case the solution of the Riemann problem is given by $P(\varrho_{t,x} = \rho) = P(\varrho_l = \rho | \varsigma > x/t)$, and in the second case, the solution of the Riemann problem is given by $P(\varrho_r = \rho | \varsigma < x/t)$, hence in both cases the solution is a conditional of the left or right initial datum. In $\mathcal{D}$, the solution is given by Eq. (28), where the two weighting terms are non-zero by definition. The random field $\varrho_{t,x}$ is a mixture of the left datum conditioned on the positivity of $\varsigma - x/t$, and the right datum conditioned on the negativity of $\varsigma - x/t$, as expressed by Eq. (28). □

The mixture nature of the solution of the Riemann problem with stochastic datum is illustrated in Fig. 2, obtained by Monte Carlo simulation with 10^5 samples, for a Greenshields flux with parameters $V = 80$ mph and $\rho_{\max} = 120$ vpm (where mph and vpm respectively stand for *miles per hour* and *vehicles per mile*), and a Riemann problem with independent uniform left and right data centered at $\rho_l = 30$ vpm, $\rho_r = 90$ vpm. Variances 100 and 400 are considered in Fig. 2 left and right respectively. The domain where the minimum of the weighting terms ($P(\varsigma > \frac{x}{t})$ and $P(\varsigma < \frac{x}{t})$) is non-zero characterizes the domain $\mathcal{D}$, and the locus of the mixture distribution.

The mixture nature of the random field is due to the stochastic nature of the shock-wave speed. Propagating a moment-based representation of the datum, as in the case of the EKF, through the deterministic model does not capture the mixture nature of the random field. The random field $\tilde{\varrho}_{t,x}$ defined by the stochastic initial datum and a deterministic Rankine–Hugoniot speed associated with the mean of the datum reads:

$$P\left(\tilde{\varrho}_{t,x} = \rho\right) = P\left(\varrho_l = \rho\right) \mathbf{1}\left(\sigma > \frac{x}{t}\right) + P\left(\varrho_r = \rho\right) \mathbf{1}\left(\sigma < \frac{x}{t}\right) \tag{29}$$

where the stochastic nature of the shock-wave speed and non-independence between the datum and the shock-wave speed

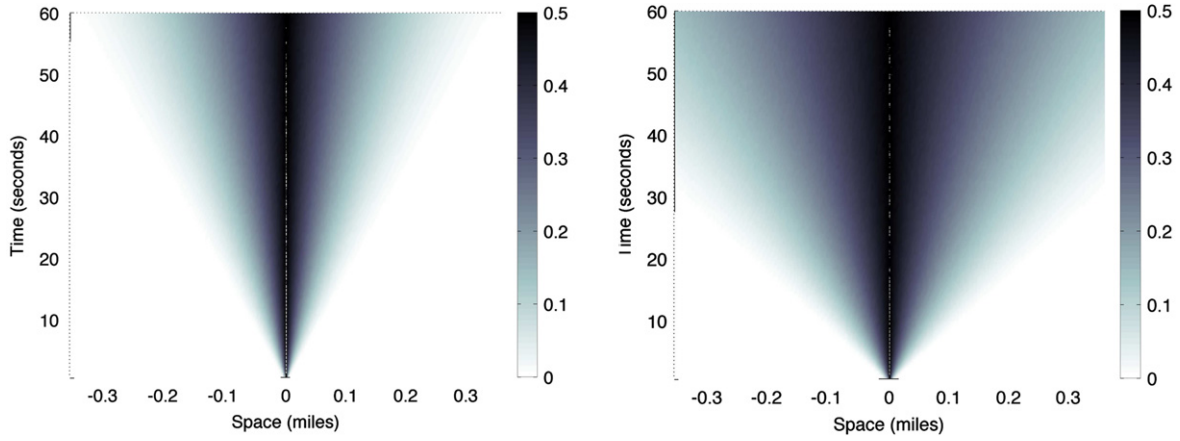

Fig. 2. *Mixture random field*: The minimum min $\left\{P(\varsigma > \frac{x}{t}), P(\varsigma < \frac{x}{t})\right\}$ is represented over space and time for additive uniform noise with zero mean and variance 100 (left) and 400 (right). The mean of the left (resp. right) datum is 30 vpm (resp. 90 vpm). As can be seen, the higher the variance on initial data, the less it is acceptable to neglect the mixture nature of the random field.

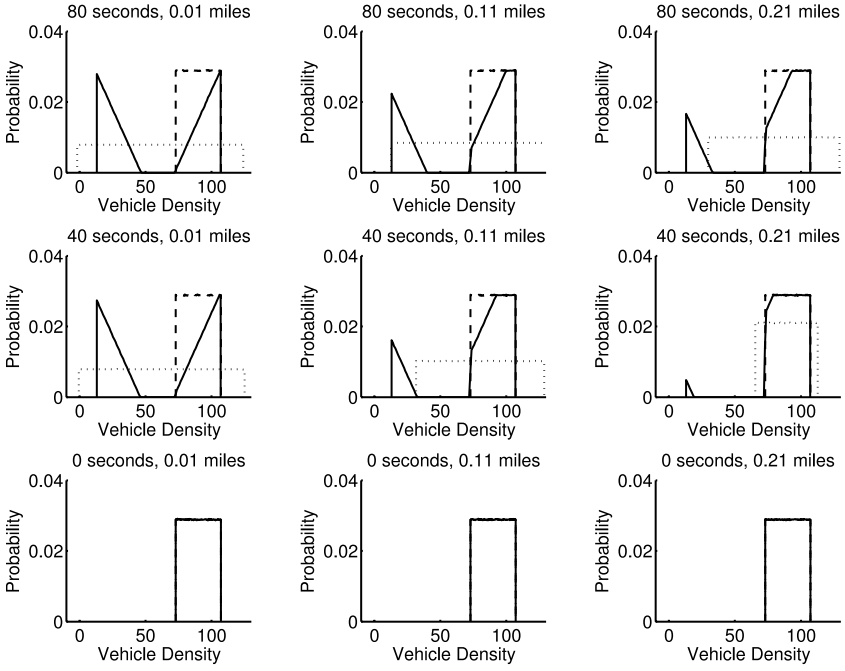

Fig. 3. *Distribution of vehicle density at different space–time locations:* Probability density function of the uncertainty $\varrho_{t,x}$ on the true state (solid line), uniform probability density function with identical mean and variance (dotted line), probability density function $\tilde{\varrho}_{t,x}$ given by a deterministic shock-wave speed between the left and right stochastic initial data (dashed line). This computation corresponds to a Greenshields fundamental diagram with uniform initial noise of variance 100. The true shock-wave is initially located at location 0 and does not move.

are neglected. The difference between the state distribution propagated in this method and the true mixture distribution is illustrated in Fig. 3, for the same model parameters and initial condition as in Fig. 2, with a variance 100 and 10^7 particles. Fig. 3 displays distributions corresponding to positive locations (0.01, 0.11, 0.21 miles), which corresponds to the right side of the left sub-figure in Fig. 2. This is a situation in which $P(\varsigma > \frac{x}{t}) < P(\varsigma < \frac{x}{t})$ (more chance for the shock to be on the left than on the right of location x at time t). This explains that the dominating mode corresponds to the right initial data. The dominating mode is the only mode represented by the random field $\tilde{\varrho}_{t,x}$, which is accurate far from the shock wave only. The correlation represented by the non-uniform distribution of the dominating mode is not captured by the random field $\tilde{\varrho}_{t,x}$. Additionally, we represent a distribution[3] with the same mean and variance as the true distribution $\varrho_{t,x}$ (which is the underlying principle of the UKF). This distribution (the dotted line) exhibits a large variance which captures the variability due to the mixture nature of the true distribution. One may note that this distribution includes negative values with non-zero probabilities, and positive values outside of the admissible range according to the model, with non-zero probabilities.

Remark 8. The solution to the stochastic Riemann problem given by Eq. (29) may be accurate if the mixture from Eq. (28)

[3] For graphical comparison, we use the same family as the initial condition, i.e. a uniform distribution (represented in dotted line in Fig. 3).

is degenerate and only one mode arises on each side of the shock wave. This is the case if the Rankine–Hugoniot speed is deterministic, which may arise in the case of specific correlated statistics or if the solution to the Riemann problem is a contact discontinuity (e.g. in the case of piecewise linear fundamental diagrams, see Proposition 4).

Proposition 3. *For a Greenshields fundamental diagram, if the left initial noise and the right initial noise are such that the sum $\rho_l + \rho_r$ is constant across all realizations ρ_l, ρ_r, then the random field $\varrho_{t,x}$ is not a mixture distribution.*

Proof. The shock-wave speed associated with realizations ρ_l, ρ_r of the Riemann datum reads:

$$\sigma_G = \frac{V\,\rho_l\left(1-\frac{\rho_l}{\rho_{\max}}\right) - V\,\rho_r\left(1-\frac{\rho_r}{\rho_{\max}}\right)}{\rho_l - \rho_r}$$

which can be rewritten as:

$$\sigma_G = V - \frac{V}{\rho_{\max}}\,(\rho_l + \rho_r)$$

which according to the assumption on the statistics is the same for all realizations ρ_l, ρ_r. The domain $\mathcal{D}$ is thus empty, and the random field $\varrho_{t,x}$ is equal to the left or right datum. □

Proposition 4. *For a triangular fundamental diagram, if $\mathcal{D}_l, \mathcal{D}_r \subseteq [0, \rho_c]$ or $\mathcal{D}_l, \mathcal{D}_r \subseteq [\rho_c, \rho_{\max}]$, the random field $\varrho_{t,x}$ is not a mixture, for almost all $(t, x) \in \mathbb{R}^+ \setminus \{0\} \times \mathbb{R}$.*

Proof. By assumption, we have $\rho_l < \rho_r$ for all realizations of the two distributions. If $\mathcal{D}_l \subseteq [0, \rho_c]$ and $\mathcal{D}_r \subseteq [0, \rho_c]$, a realization σ_T of the shock-wave speed ς_T for the triangular diagram reads:

$$\sigma_T = \frac{Q(\rho_r) - Q(\rho_l)}{\rho_r - \rho_l},$$

which can be rewritten using expression (16) and the fact that $\rho_l \in \mathcal{D}_l$, $\rho_r \in \mathcal{D}_r$, as:

$$\sigma_T = \frac{\rho_l V - \rho_r V}{\rho_l - \rho_r} = V$$

which yields a shock-wave speed equal to the free-flow speed for all realizations. Therefore the shock-wave speed is deterministic, and the random field solution of the Riemann problem is unimodal for almost all $(t, x) \in \mathbb{R}^+ \setminus \{0\} \times \mathbb{R}$. Similarly if $\mathcal{D}_l, \mathcal{D}_r \subseteq [\rho_c, \rho_{\max}]$, the shock-wave speed is the speed of backward moving waves w. The domain $\mathcal{D}$ is thus empty, and the random field $\varrho_{t,x}$ is equal to the left or right datum. □

Consequently, for estimation using the CTM, when the traffic state is completely in free-flow ($\mathcal{D}_l, \mathcal{D}_r \subseteq [0, \rho_c]$) or completely in congestion ($\mathcal{D}_l, \mathcal{D}_r \subseteq [\rho_c, \rho_{\max}]$), the estimate distributions on the left and on the right do not mix and the normality assumption of the initial condition estimates propagates (this conditional linearity of the dynamics is used by the MKF).

5.2. Mixture solutions to the Godunov scheme

In this section, we analyze numerically how the emergence of mixture distributions in the solution of the Riemann problem for the stochastic datum relates to the emergence of mixture distributions in the solution to the Godunov scheme. The Godunov scheme computes a numerical solution to the Cauchy problem on a discretization grid, by iteratively solving Riemann problems between neighboring cells and averaging their solutions within each cell. Numerical estimates produced in this manner differ from the estimates obtained by solving the Riemann problem on a continuous domain, due to numerical diffusion introduced in the averaging step and the discrete setting. Additionally, in the intent of modeling numerical diffusion, discretization error and inherent modeling error, it is common practice [2] to introduce an additive random source term to the discretized PDE (18). In order to study the emergence of mixture distributions in this context, we propose the following numerical experiments.

We consider the Greenshields fundamental diagram with parameters $V = 80$ mph, $\rho_{\max} = 120$ vpm, and the stochastic Riemann datum ($\varrho_l = \mathcal{N}(30, 100)$, $\varrho_r = \mathcal{N}(90, 100)$) (we truncate the normal distribution to force its support into the admissible domain $[0, \rho_{\max}]$ of the model). Using Monte Carlo simulations with 10^5 samples, we compute the (continuous) solution of the Riemann problem and the (discrete) solution of the Godunov scheme with *Courant–Friedrichs–Lewy* (CFL) [67] condition equal to one, spatially uniform left and right realizations of initial noise, and for various discretization grid sizes and values of the model noise.

Numerical diffusion: The influence of numerical diffusion on continuous and discrete numerical estimates (see Fig. 4) is assessed by comparing the solution to the Riemann problem (solid line) with the solution to the Godunov scheme on a coarse grid (six space cells, 18 time-steps, dashed line) and on a fine grid (12 space cells, 36 time-steps, dotted line). The Monte Carlo simulation is run with 10^5 samples. As illustrated in Fig. 4, comparison of the numerical solutions on different grids illustrates that diffusion in the Godunov scheme smoothens the mixture nature of the solution to the Riemann problem. The numerical solution exhibits two modes but due to diffusion, a non-zero probability arises between the two modes. This illustrates that by discretization of the constitutive model, the true nature of the distribution of uncertainty is blurred. This is not necessarily a problem if the discrete numerical model (Godunov scheme in this case) is considered to be the physical model, i.e. is considered to represent the dynamics of the true state, as commonly done in transportation. However, it shows the limitation of discrete approaches for estimation with continuous physical models, such as the LWR PDE.

Model noise: We propose to compare (see Fig. 5) the continuous solution to the Riemann problem (solid line), the discrete solution to the Godunov scheme with no model noise (dotted line), and model noise represented by a random variable $\mathcal{N}(0, 50)$ (dashed line), on a grid with six space cells and 18 time-steps. The addition of a model noise term to the Godunov scheme to account for model errors leads to a reduction of the mixture nature of the distribution solution to the stochastic Riemann problem. It induces a diffusion of the true distribution, which contributes to further smoothen the two components of the mixture (see Fig. 5). This diffusion is more structured that pure numerical diffusion (see Fig. 4), but this example clearly advocates for noise modeling in order to account specifically for discretization error as a function of the state and the corresponding distribution of uncertainty [87–89].

Lack of correlation: The existence of mixture distributions around the discontinuity creates a correlation between the two sides of the shock wave (see Fig. 6). By propagating a single component of the mixture on each side of the shock wave, the covariance structure is misrepresented by the linearized model. This is illustrated in Fig. 6 representing the covariance structure of the estimate at time-step 20, for a Monte Carlo simulation with 10^4 particles in the left sub-figure, and for the linearized model in the right sub-figure. The fundamental diagram is a Greenshields fundamental diagram with parameters $V = 80$ mph, $\rho_{\max} = 120$ vpm, and the stochastic Riemann datum corresponds to ($\varrho_l = \mathcal{N}(15, 100)$, $\varrho_r = \mathcal{N}(75, 100)$), in vehicles per mile. This corresponds to a shock wave moving forward, starting at time 0 from cell 0. One may note that due to the CFL condition, at time 20, no physical correlation can exist farther than 20 cells around

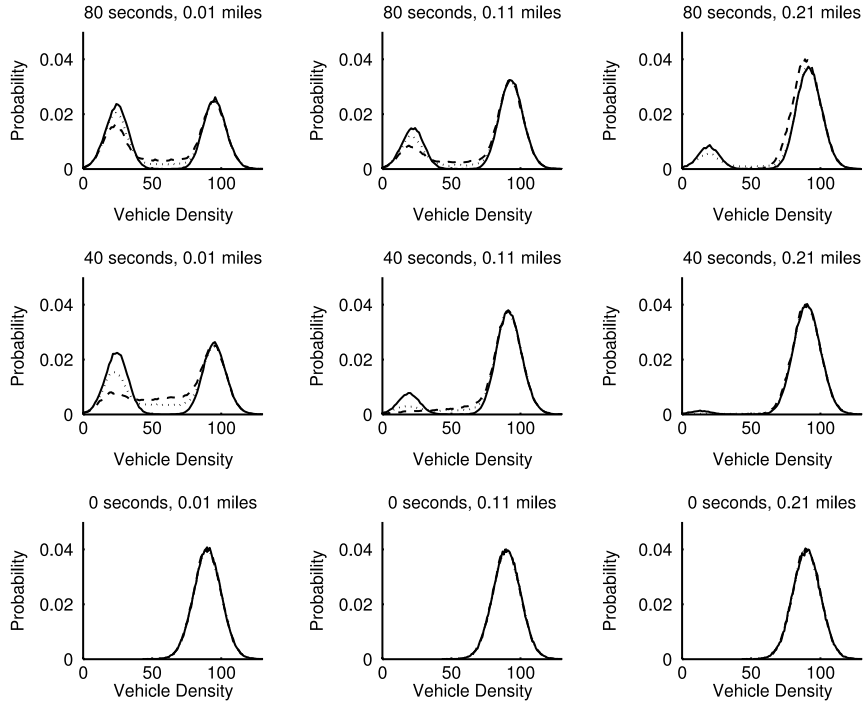

Fig. 4. *Numerical diffusion:* The mixture nature of the solution of the Riemann problem (solid line) is more accurately captured by the numerical solution with low numerical diffusion (dotted line) computed on the fine grid than by the numerical solution with high numerical diffusion (dashed line) computed on the coarse grid.

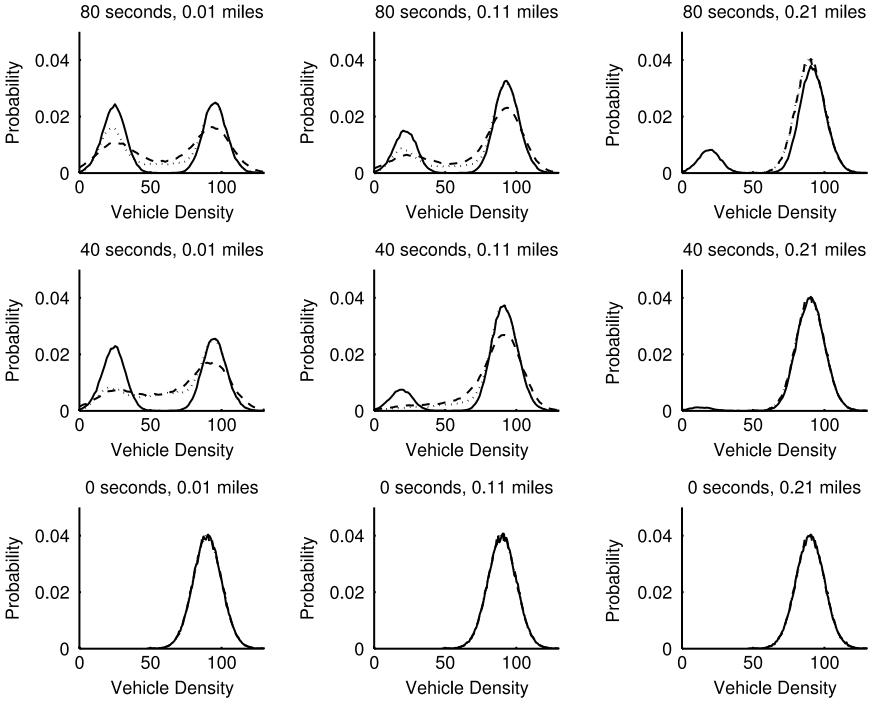

Fig. 5. *Model noise:* the probability density function of the solution of the Riemann problem is represented by a solid line, the probability density function of the solution of the Godunov scheme with no noise is represented by a dotted line, the solution of the Godunov scheme with Gaussian centered model noise with variance 50 is represented by a dashed line.

the diagonal. The block diagonal structure of the linearized model estimate at the shock wave appears clearly, whereas for the Monte Carlo simulation with 10^4 particles, the state error covariance matrix is band diagonal, which illustrates the correlation between the two sides of the shock wave due to the mixture components. The comparison between the two figures displays the lack of correlation, across the shock, of the covariance given by the linearized model. In the absence of correlation, measurements realized on one side of the shock do not influence the estimate on the other side of the shock. The fact that the linearized model overestimates the variance around cells neighboring the discontinuity location is visible from the color scale.

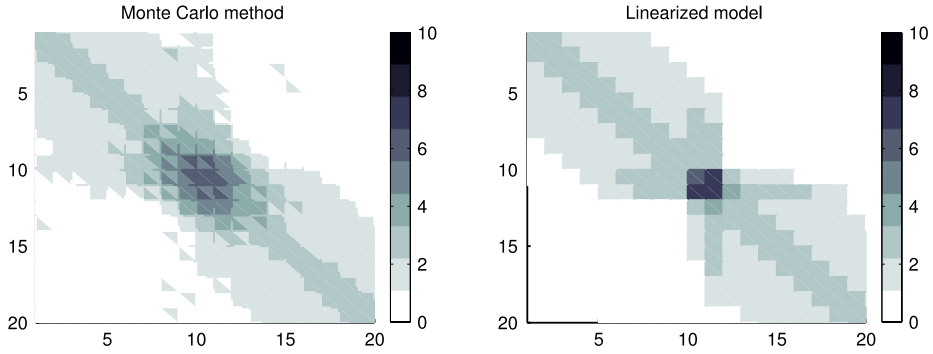

Fig. 6. *State error log-covariance matrix*: The shock wave is located at cell 10. The logarithm of the absolute value of the state error covariance matrix given by a Monte Carlo simulation with 10^4 particles (left) illustrates significant correlation between the two sides of the discontinuity, due to the existence of mixture distributions. The state error covariance given by a linearized model (right) is block-diagonal at the shock wave, due to the lack of correlation between the two sides of the shock wave in the linearized model. This lack of correlation might be problematic for estimation, because measurements might not give information across shocks.

5.3. Discussion

In this section, we discuss how the properties of the distribution of the uncertainty on the true state solution of the Riemann problem with stochastic datum relate to the accuracy of the estimate given by classical filters at the analysis step.

Forecast mean: The estimate given by the mean of the distribution obtained by deterministic propagation of the mean of the left and right data (case of EKF), with additive model noise, seems biased since it only captures one component of the mixture (see Fig. 3 as well for instance). Close to the shock wave, the diffusivity of the Godunov scheme numerically alleviates this drawback by smoothing the mixture through diffusion. The bias at the shock wave due to mixture uncertainty is less likely to occur with sample-based filters which implicitly consider a stochastic model through the propagation of samples by a deterministic model (see experiments below). We reemphasize here that the true shock-wave speed for Figs. 3 and 4 is zero, hence the true shock wave does not move from location 0.

Forecast variance: As illustrated in Fig. 3, close to the shock wave, even when the mean and the variance of the uncertainty on the true state are propagated accurately, representing the mixture distribution of the uncertainty by a unimodal distribution leads to considering a variance corresponding to the two modes, hence a greater dependency on the observations at the analysis step, through an increased gain, which is due to a poor representation of the uncertainty related to the prior distribution. On the other hand, if only a single mode of the uncertainty is accurately captured (case of EKF), the estimate exhibits a lower variance than the uncertainty, which is a classical cause of divergence of the filter.

Analysis step with mixture uncertainty: We consider the case of a stationary shock wave with left and right initial data ($\varrho_l = \mathcal{N}(30, 100)$, $\varrho_r = \mathcal{N}(90, 100)$), for a Greenshields fundamental diagram with parameters $V = 80$ mph, $\rho_{\max} = 120$ vpm. The true stationary shock wave is located at location 20.5 throughout each simulation. Figs. 7 and 8 display the prior and posterior true uncertainty, and respectively the normal distributions corresponding to the EKF estimate and the EnKF ensemble estimates[4], as well as the observations. The prior distribution of the uncertainty on the true state is computed by Monte Carlo simulation with 10^5 particles, and its posterior obtained by full Bayesian update. We study the characteristics of the analysis step of the EKF and the EnKF, at different times, with a single observation with observation noise variance 100. The posterior computed by the analysis is not propagated further but simply displayed. This means that each row in Figs. 7 and 8 corresponds to a different value of the true state, a different realization of the observation noise, and a single analysis step. For the sake of comparison we always sample an observation at location 21.

The sensitivity of the filters to the observation is illustrated by the significant difference between the prior and the posterior (respectively dotted and dashed lines), around the shock wave, for both the EKF and the EnKF. At the location of the observation (location 21), the prior provided by the EKF, which only captures a single mode, is more inaccurate than the prior given by the EnKF, which can account partially for mixture distributions representation with ensemble members. However, after analysis, the posteriors for the two filters are very similar at the location of the observation. Away from the shock wave (location 19 and 22), it is clear that the EKF estimate exhibits a non-consistent error variance (simulations 1, 2, 3 in particular).

The correlation across the shock wave clearly discriminates the two filters. Across the shock wave, at location 20, the posterior given by the EKF (dashed line) is often centered on the wrong mode of the posterior uncertainty (dash–dotted line). This is not the case for the EnKF which captures the two modes of the mixture in most cases. When the observation corresponds to a mode of the mixture uncertainty not well represented by the estimate (for instance run 2, location 21 of Fig. 7), it can be noted that the posterior distribution can provide more inaccurate estimate than the prior; for instance the posterior given by the EKF (dashed line) for run 2, location 20, is outside the range of values represented. This illustrates the difficulty of capturing true correlation induced by mixture uncertainty across the shock wave.

The mixture nature of the uncertainty is clearly reduced by the observation, however, the two modes are still present and propagate in the posterior uncertainty (dash–dotted line at location 19 and 20 for simulation 1, location 22 for simulation 2, location 20 for simulation 3).

These numerical examples illustrate the limitations of the suboptimal MMSE estimates provided by the EKF and EnKF, in the case of mixture distributions arising in traffic flow around shock waves. Stochastic filters such as the EnKF are more robust to the mixture nature of the uncertainty, since their sample representation allows them to better capture the full variance of the two modes of the distribution of the uncertainty on the true state. However, this leads to higher sensitivity of the filter and may lead to instabilities at shock waves. On the other hand, deterministic filters able to capture only a single mode of the distribution of the uncertainty on the true state exhibit a lower variance than the uncertainty, which may cause divergence of the estimate if the models have low error terms.

[4] Even though the EnKF propagates and updates ensemble, for visual consistency in a context of minimum variance estimation, and due to the low number of ensemble members used, we present the normal distribution corresponding to the ensemble members distribution.

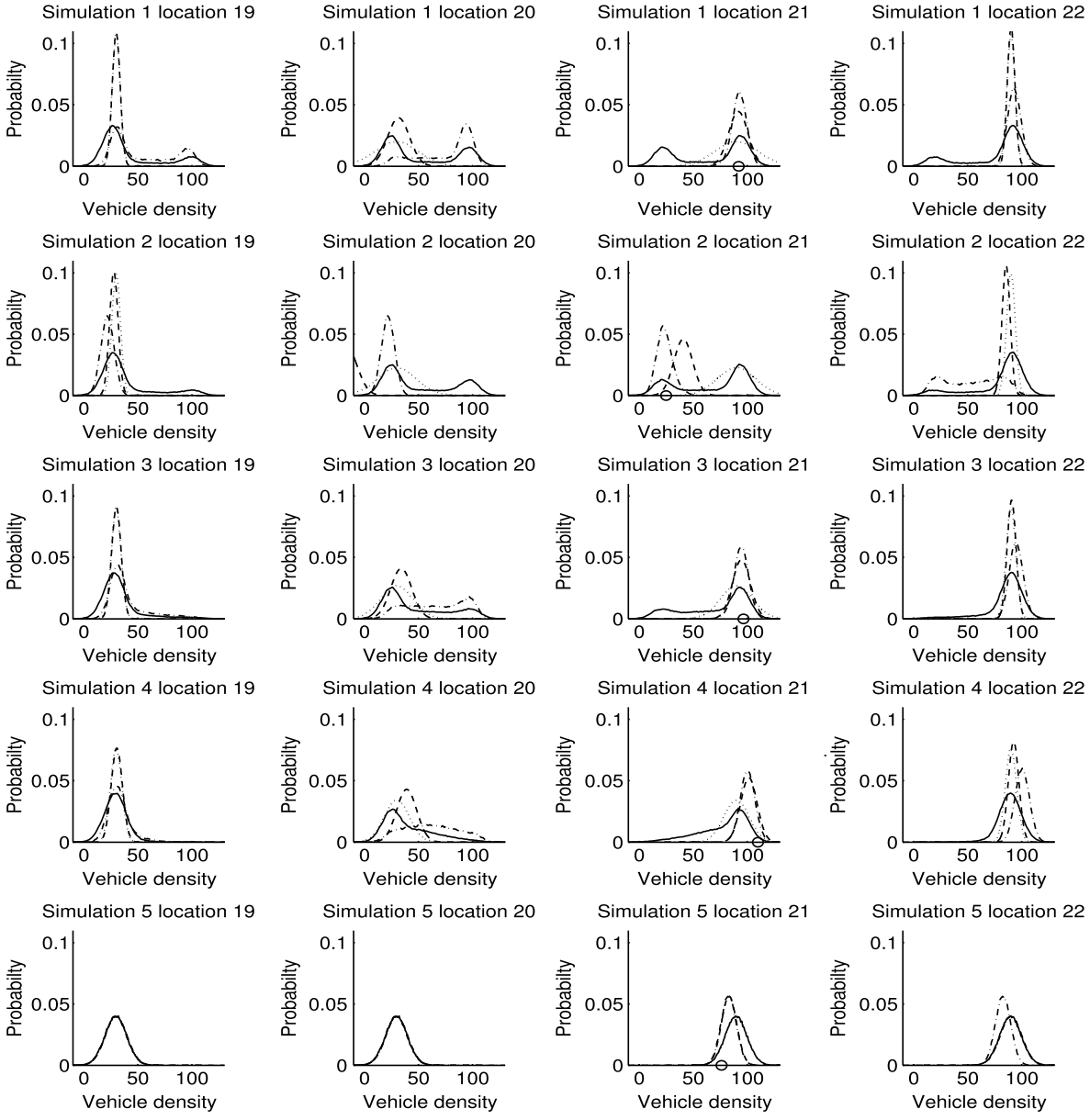

Fig. 7. *EKF analysis step:* the analysis step at different times is represented for a stationary shock wave at location 20.5, between 30 and 90 vpm, initial condition noise variance 100, and observation noise variance 100. The observation is represented by a circular marker. The prior distribution of the uncertainty on the true state obtained by Monte Carlo simulation with 10^5 samples is represented by a solid line, the posterior distribution obtained by Bayesian update is represented by a dash–dotted line. The prior distribution given by propagation through the linearized model is represented by a dotted line, and the posterior distribution given by the analysis step of the EKF is represented by a dashed line.

6. Model non-differentiability

In this section, we show that the numerical Godunov flux defined in (18)–(19) is non-differentiable. We prove that consequently, the discrete-time dynamics of the Godunov scheme is non-differentiable, which prevents straightforward application of filtering algorithms requiring differentiability to discrete transportation models based on the Godunov scheme.

6.1. Characterization of non-differentiability domain

The Godunov scheme consists of a dynamical system (18) resulting from the discretization of the transport equation (14) where the numerical flux $q_G(\cdot,\cdot)$ can be defined in a piecewise manner on regular sub-domains in the case of a concave flux with a single maximum (19). The following proposition states the lack of continuous differentiability at a specific boundary between two of these sub-domains.

Proposition 5. *On the domain $\mathcal{S}$ defined as:*

$$\mathcal{S} = \left\{(\rho_l, \rho_r) \in [0, \rho_{\max}]^2 \mid \rho_l < \rho_r \text{ and } Q(\rho_l) = Q(\rho_r)\right\}, \tag{30}$$

the numerical Godunov flux (19) is not differentiable.

Proof. The expression of the numerical Godunov flux is given by Eq. (19). In each sub-domain of definition corresponding to each line of (19), if the flux function $Q(\cdot)$ is differentiable, the numerical flux $q_G(\cdot,\cdot)$ is also left and right differentiable. It is straightforward to compute its left and right derivative on each sub-domain:

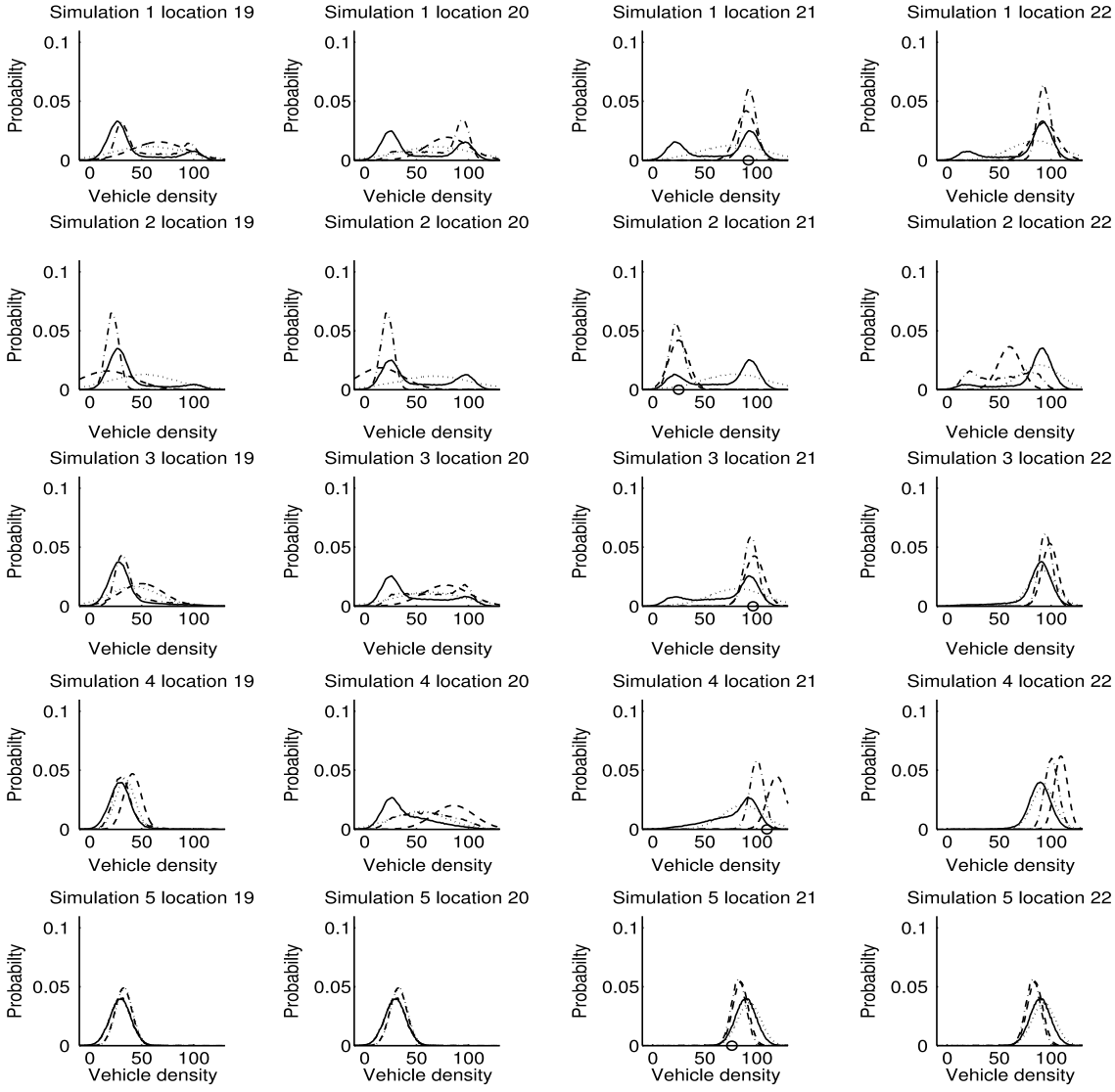

Fig. 8. *EnKF analysis step:* the analysis step at different times is represented for a stationary shock wave at location 20.5, between 30 and 90 vpm, initial condition noise variance 100, and observation noise variance 100. The observation represented by a circular marker. The prior distribution of the uncertainty on the true state obtained by Monte Carlo simulation with 10^5 samples is represented by a solid line, the posterior distribution obtained by Bayesian update is represented by a dash–dotted line. The estimate distributions given by the EnKF are represented as normal distributions with corresponding mean and variance. The prior given by propagation of 40 ensemble members is represented as a normal distribution by a dotted line, and the posterior given by the analysis step of the EnKF is represented as a normal distribution by a dashed line.

$$\frac{\partial q_G}{\partial \rho_l}(\rho_l, \rho_r) = \begin{cases} Q'(\rho_l) & \text{if } \rho_r \le \rho_l < \rho_c \\ 0 & \text{if } \rho_r \le \rho_c \le \rho_l \\ 0 & \text{if } \rho_c < \rho_r \le \rho_l \\ \begin{cases} Q'(\rho_l) & \text{if } Q(\rho_l) < Q(\rho_r) \\ 0 & \text{if } Q(\rho_l) > Q(\rho_r) \end{cases} & \text{if } \rho_l < \rho_r \end{cases} \tag{31}$$

$$\frac{\partial q_G}{\partial \rho_r}(\rho_l, \rho_r) = \begin{cases} 0 & \text{if } \rho_r \le \rho_l < \rho_c \\ 0 & \text{if } \rho_r \le \rho_c \le \rho_l \\ Q'(\rho_r) & \text{if } \rho_c < \rho_r \le \rho_l \\ \begin{cases} 0 & \text{if } Q(\rho_l) < Q(\rho_r) \\ Q'(\rho_r) & \text{if } Q(\rho_l) > Q(\rho_r) \end{cases} & \text{if } \rho_l < \rho_r. \end{cases} \tag{32}$$

As indicated by the fourth case of Eq. (31) (or equivalently for the right derivative with the fourth case of Eq. (32)), the left derivative of the numerical flux is only defined on the left and on the right of the domain $\mathcal{S}$ defined by Eq. (30), with the left value being $Q'(\rho_l)$ and the right value being 0. The left and right values are equal only at the capacity point (point of maximal flux), in the case of a flux differentiable at capacity. Since the left derivative is not differentiable on $\mathcal{S}$, the numerical flux is not differentiable on its domain of definition. □

The domain of non-differentiability of the numerical Godunov scheme corresponds to the locus of stationary shock waves. In particular, the numerical Godunov flux and the discrete dynamics associated with the Godunov scheme are differentiable at moving shock waves. In the case of discretization schemes with higher numerical viscosity, for instance the *Lax–Friedrichs* numerical scheme [67], differentiability is obtained everywhere but numerical approximation of discontinuities is less accurate.

Proposition 6. *The discrete time dynamics of the Godunov scheme is non-differentiable, and in the case of a differentiable flux function $Q(\cdot)$, the non-differentiability domain consists of the locus $\mathcal{S}$ of stationary shock waves.*

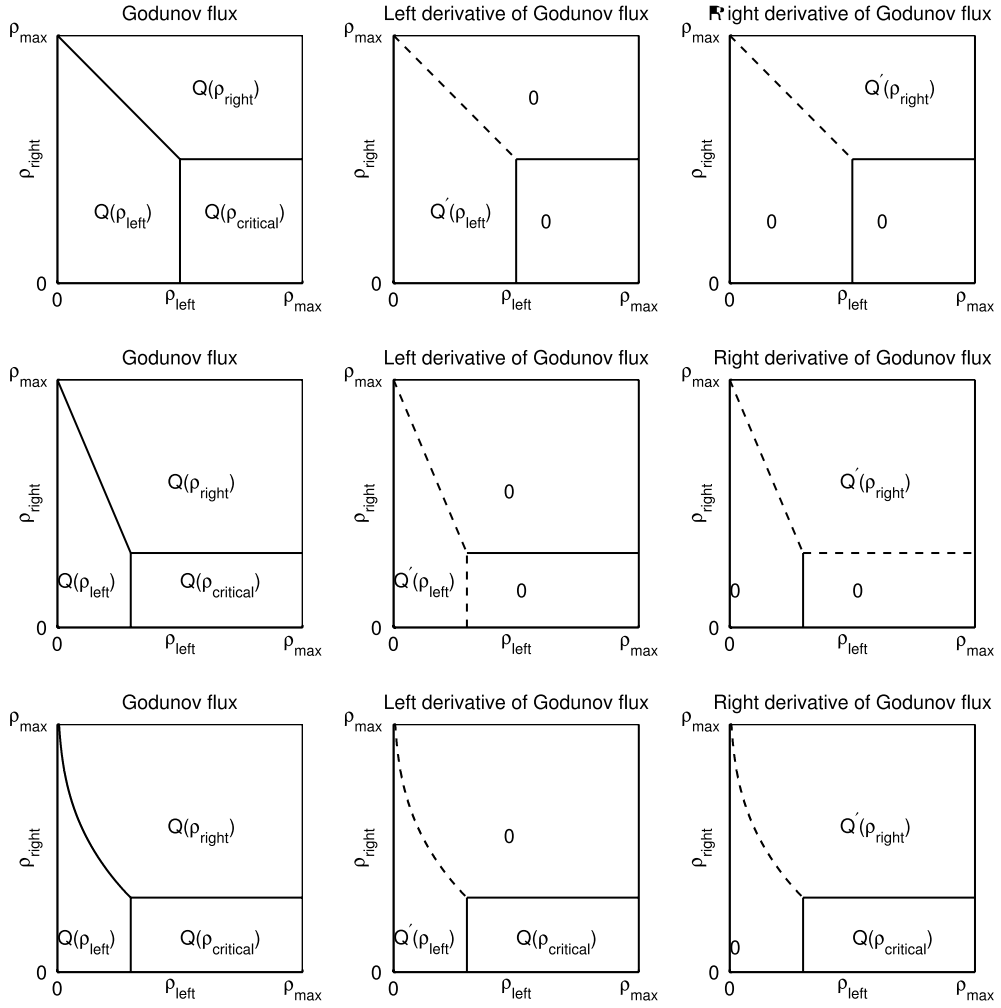

Fig. 9. *Locus of non-differentiability of the numerical Godunov flux*: The top, middle and bottom rows respectively correspond to the Greenshields, triangular, and exponential fundamental diagrams. The Godunov flux is defined in a piecewise manner on the three sub-domains delimited by solid or dashed lines. A dashed line indicates discontinuity across the boundary of the domain, whereas a solid line indicates continuity at the boundary. The three diagrams exhibit non-differentiability of the locus of stationary shock waves (center and right column, oblique curve). Additionally, the triangular diagram (middle row) exhibits non-differentiability at the critical density.

Proof. The numerical flux is non-differentiable in the domain $\mathcal{S}$ defined by (30). Since it is impossible to have at the same time $(\rho_{i-1}^n, \rho_i^n) \in \mathcal{S}$ and $(\rho_i^n, \rho_{i+1}^n) \in \mathcal{S}$, the discrete time dynamics defined by (18) is non-differentiable. In the case of a differentiable flux function $Q(\cdot)$, the numerical flux is also differentiable in all its sub-domains of definition, and it can be checked in Fig. 9 that it is also continuously differentiable at their boundaries, thus $\mathcal{S}$ is the non-differentiability domain of the discrete time dynamics associated with the Godunov scheme. □

The non-differentiability of the discrete dynamics associated with the Godunov scheme does not result from a numerical issue but results from the structure of the solution of the continuous partial differential equation considered. This can be verified by considering the solution to the Riemann problem in the case of a stationary shock wave. The solution that consists of upstream and downstream densities with equal fluxes is stationary. However, it is clear that a slight perturbation of the upstream or downstream density causes the shock wave to propagate and the domain corresponding to the left or right initial condition to eventually prevail, depending on the flux balance at the discontinuity.

Remark 9. In the case of non-differentiable flux functions $Q(\cdot)$ such as the triangular flux function or the Smulders flux function, it is clear that the dynamics of the numerical solution is not differentiable. However, since the flux function results from an empirical fit, the flux function can be approximated by a smooth function with relatively small consequences. The non-differentiability described in Proposition 5 results from the intrinsic properties of the conservation law, which can only be fixed by modifying the constitutive physical principles of the model.

Remark 10. For junction problems modeled as the maximization of a linear objective function of the traffic state under linear inequality constraints (see Remark 3), the optimum is always attained at a vertex of the constraint polytopes, hence the flow through the junction is not a differentiable function of the traffic state and the same difficulties happen there as well.

6.2. Numerical experiments

In this section, we analyze the estimation error induced by the lack of differentiability of the numerical Godunov flux at the locus of stationary shock waves.

For clarity we present results for the case of the Greenshields flux function (15) (with parameters $V = 80$ mph and $\rho_{\max} = 120$ vpm, as in the previous section), which is differentiable on its domain of definition. Similarly, in order to simplify the analysis, we consider only initial condition noise, drawn from i.i.d. normal distribution $\mathcal{N}(0, 100)$. The model noise is considered to be 0. We use the Godunov scheme (18), with CFL condition [67] equal to 1,

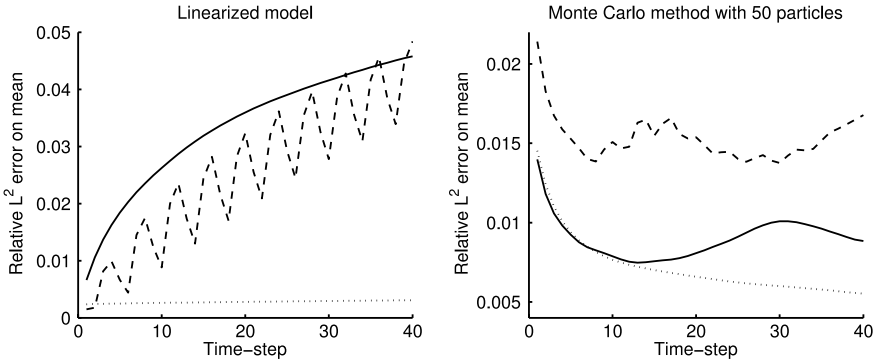

Fig. 10. *Mean error growth*: the growth with time of the relative L^2 error on the mean is represented for a linearized model (left) and a Monte Carlo simulation with 50 particles (right). The solid line corresponds to the case of a stationary shock wave with $\rho_l = 30$ vpm, $\rho_r = 90$ vpm, the dashed line corresponds to the case of a moving shock wave, with $\rho_l = 15$ vpm, $\rho_r = 75$ vpm, the dotted lined corresponds to the case of a rarefaction wave, with $\rho_l = 90$ vpm, $\rho_r = 30$ vpm.

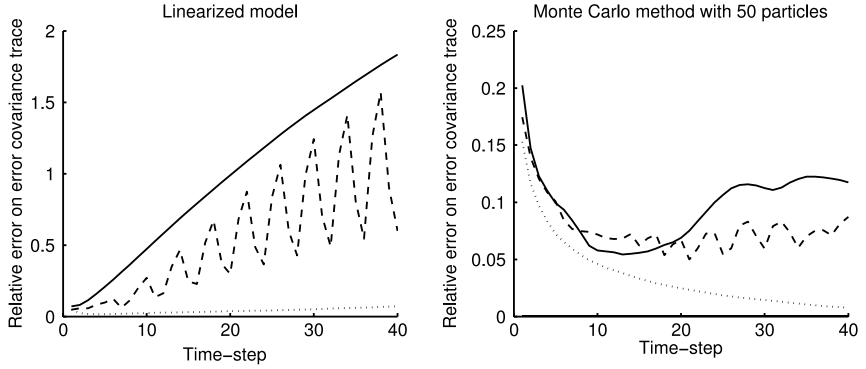

Fig. 11. *Covariance error growth*: the growth with time of the relative error on the error covariance trace is represented for a linearized model (left) and a Monte Carlo simulation with 50 particles (right). The solid line corresponds to the case of a stationary shock wave with $\rho_l = 30$ vpm, $\rho_r = 90$ vpm, the dashed line corresponds to the case of a moving shock wave, with $\rho_l = 15$ vpm, $\rho_r = 75$ vpm, the dotted lined corresponds to the case of a rarefaction wave, with $\rho_l = 90$ vpm, $\rho_r = 30$ vpm.

and 80 cells in space. The distribution of the uncertainty on the true state is computed using a Monte Carlo simulation with 10^4 particles, and the forecast moments using different propagation models are compared against the true moments. In order to assess the accuracy of the estimate covariance, we compute two error metrics. The error metric for the mean, in Fig. 10, is the relative L^2 error:

$$\frac{\|\mu_e - \mu\|_2}{\|\mu\|_2}$$

where μ_e denotes the estimated mean using the forecast step of a model, and μ is the true forecast. The error metric for the covariance, in Fig. 11, is the relative absolute error on the error covariance trace, defined by:

$$\frac{\mathrm{trace}(|\tilde{\Sigma} - \Sigma|)}{\mathrm{trace}(\Sigma)}$$

where $\tilde{\Sigma}$ denotes the estimated error covariance given by the forecast model and Σ denotes the true error covariance.

Estimate error: The error induced by the use of a linearization method at the locus of the stationary shock wave is illustrated by a solid line in Fig. 10 for the mean and in Fig. 11 for the covariance, for the use of the derivative of the numerical Godunov flux on the left at its point of non-differentiability. For state propagation using a Monte Carlo method with 50 particles (right sub-figure) or the linearized model (right sub-figure), the shock waves lead to the highest error, which is due to the fact that only entropic shock waves are propagated by the scheme; the uncertainty associated with the initial condition propagates toward the shock-wave location. In the case of a rarefaction, the uncertainty associated with the initial datum propagates outward, and the centered fan is deterministic.

The state error covariance given by forward simulation using the linearized dynamics diverges in time from the covariance of the uncertainty on the true state (see Fig. 11 left). In the case of a stationary shock wave (solid line), the divergence is slightly faster than in the case of a moving shock wave. In particular, noting that the oscillations in the curve associated with a moving shock wave (dashed line) in Fig. 10 and Fig. 11 correspond to a change of cells and that the meaningful error for this phenomenon corresponds to the lower envelope of this curve, the divergence associated with the stationary shock wave is noticeably greater. However, one may note that Fig. 10, left, and Fig. 11, left, only correspond to considering the derivative on the left at the non-differentiability locus. Different weightings of the left and right derivative at the non-differentiability domain might lead to better results.

6.3. Discussion

In this section we analyze the consequences of non-differentiability of the dynamics of the Godunov scheme for state estimation.

As illustrated in Fig. 10 left, the trend of the estimation error due to model nonlinearity is comparable for the stationary shock wave (solid line) and for the moving shock wave (dashed line). This is consistent with the fact that the propagation of the estimate mean in the linearized model does not involve differentiability. The error introduced is simply due to the nonlinearity of shock waves with the Greenshields flux function. In the case of the rarefaction wave (dotted line), the estimation error is much smaller due to the entropy condition and the fact that information propagates outward from the initial discontinuity.

For a moving shock wave (dashed line), the error exhibits a typical oscillation feature due to error of location of the shock wave. The increasing part of the oscillation corresponds to the

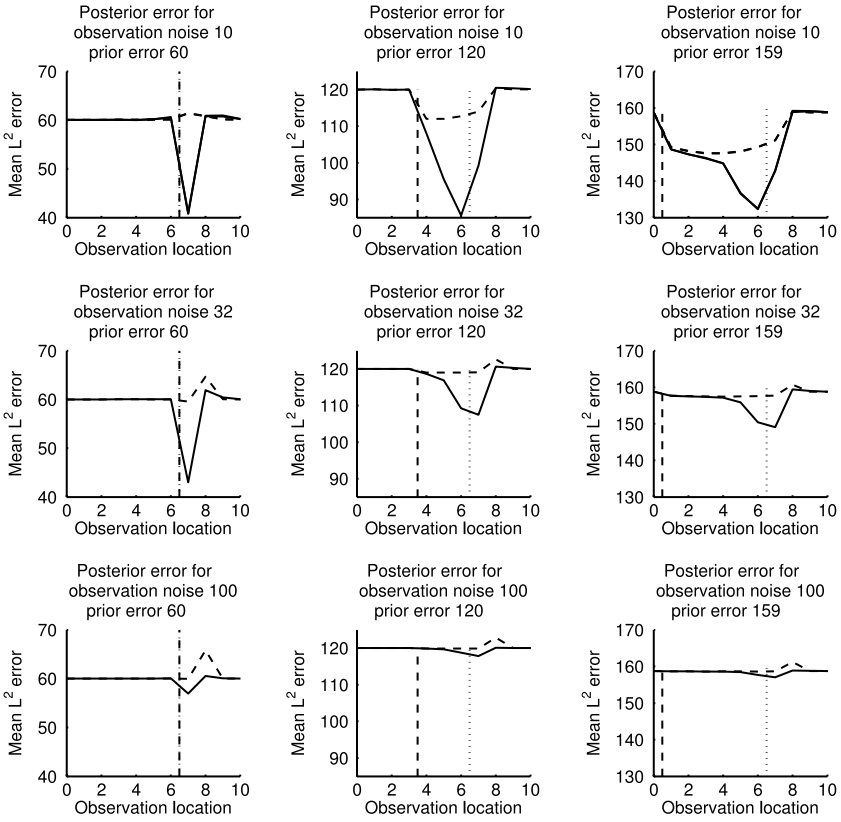

Fig. 12. *Posterior mean error*: the mean L^2 error of the posterior for 10^3 draws of the observation at each location, is represented as a function of the observation location for an analysis with prior covariance obtained by Monte Carlo simulation with 10^4 samples (solid line), and for an analysis with prior covariance propagated by the linearized model (dashed line). Top, middle, and bottom row respectively correspond to observation noise standard deviation of 10, 32, and 100. The prior shock wave, represented as a vertical dotted line, is located between cells 6 and 7 for all simulations. For the left, middle, and right columns, the true shock wave, represented as a vertical dashed line, is respectively located between cells 6 and 7, 3 and 4, and 0 and 1.

mixture nature of the distribution of the uncertainty arising in the cell where the shock wave will move, hence increasing the error with the linearized model. The decreasing part of the oscillation corresponds to the shock wave actually propagating to the cell, and reducing the error. The finite slope on the decreasing part corresponds to the effect of diffusion.

The non-differentiability of the numerical flux introduces an error in the error covariance which increases with time at a rate noticeably greater than the error growth rate in the error covariance for a moving shock wave (see Fig. 11 left in which the trend of the solid line is comparable to the trend of the top of the peaks of the dashed line).

Inaccurate estimation of the state covariance at the forecast step, depicted in Fig. 11, impacts the use of measurements at the analysis step. This is illustrated in Fig. 12, in which we consider an analysis done at time 40, for the case of the stationary shock wave, with the same parameters used in Fig. 11. We compare the posterior error covariance computed by the analysis step defined by the Kalman filter (5), with on one hand a covariance computed by propagation of the initial condition covariance through the linearized state model, and on the other hand a covariance computed by a Monte Carlo simulation with 10^4 samples. The prior means and the observations are identical for both cases, hence the discrepancy in the posteriors is solely due to the discrepancy in the prior covariances and results from the inaccuracy of the covariance propagated by the linearized non-differentiable model. A Monte Carlo simulation with 10^4 samples is considered to provide the distribution of the uncertainty on the true state.

As illustrated in Fig. 12, the error associated with the prior covariance induces an error in the posterior mean. In particular, for observations close to the discontinuity, one can note that the error in the posterior can be higher than the prior error, which corresponds to the horizontal line. The inability to capture the covariance structure at the shock wave, presented in the previous section, is also visible in the case of an accurate prior (left column) with a different posterior error for observations located on the left or on the right of the shock wave, although the problem is symmetric, as illustrated by the posterior error for the true covariance error in that case.

The fact that the filter may diverge due to the wrong covariance structure propagation by the linearized non-differentiable model is illustrated in Fig. 13 in which we present the posterior covariance for the two different analyses described above, on one hand with the covariance propagated by the linearized model, and on the other hand with the covariance associated with the true distribution of uncertainty, computed using a Monte Carlo simulation with 10^5 samples and the parameters of Fig. 12 left column.

For observation with low error located close to the shock-wave location, the analysis can cause the linearized filter to diverge by introducing a covariance lower than the covariance on the uncertainty. This echoes the analysis on the nonlinearity and the difficulty to model correctly the correlation structure at shock waves. In particular it is clear that observations away from shock waves do not particularly improve the estimates, and observations close to shock waves can potentially decrease the accuracy of the estimates and performance of the filter at the next time step.

7. Conclusion

In this article, we showed that the classical scalar macroscopic traffic models based on the Lighthill–Whitham–Richards partial

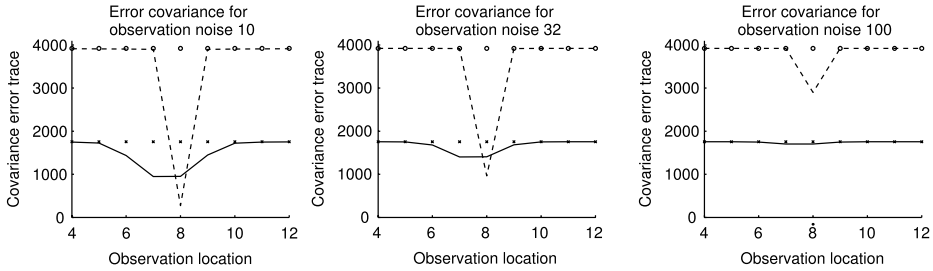

Fig. 13. *Posterior covariance error*: the posterior covariance for the linearized model (dashed) and for the Monte Carlo simulation with 10^5 samples (solid) with respective prior covariance as circle and cross, are represented as a function of the observation location.

differential equation exhibit fundamental dynamical properties which are not accounted for by classical filtering methods derived from the Kalman filter. It is a problem in practice, since these features are essential for the proper characterization of traffic flow patterns, in particular shock waves and standing waves. We focused our analysis on the Riemann problem and studied analytically and numerically the typical features introduced in the distribution of the uncertainty on the true state by nonlinear and non-differentiable dynamics.

We showed analytically that the nonlinearity of traffic causes the uncertainty in the state to translate into uncertainty in shock-wave speed and location, which yields mixture distribution at the true location of the shock wave. This is a phenomenon that the extended Kalman filter, unscented Kalman filter and ensemble Kalman filter assumptions do not account for. We provided analytical computations of the resulting errors in the estimate distributions provided by filters using either deterministic distribution moment propagation (extended Kalman filter) or sample-based distribution moment propagation (ensemble Kalman filter). We discussed the resulting estimation errors caused by misrepresenting the estimate as a unimodal distribution. Numerical computations of the solution to the discretized partial differential equation using the Godunov scheme were proposed to critically assess the validity of these conclusions for discretized models with additional modeling error.

We proved that for differentiable fundamental diagrams, the Godunov dynamics is non-differentiable at the locus of stationary shock waves, which may arise for all density–flow relationships which are not monotonic. We also showed that this non-differentiability is the cause for additional estimation error when using a filter requiring computation of the Jacobian of the dynamics (such as the extended Kalman filter).

Finally, we numerically demonstrated that some of these drawbacks of classical filters are alleviated in the presence of large modeling errors and very limited when using the triangular fundamental diagram, and consequently the cell-transmission model, which exhibits a piecewise linear relationship between density and flow.

Traffic estimation heavily depends on precise model calibration, and accurate noise modeling. Our analysis, which considered the difficulties associated with filtering for true state models, presented new findings on the statistics of the uncertainty on the true state even with smooth and normal initial conditions. These results illustrate that the specific properties of traffic flow may justify considering filters based not only on the first two moments of the distribution, but on more complex distribution representations, and using full model propagation. For different applications and depending on the volume and accuracy of trusted measurements available, new filters able to account for these complex traffic-dependent statistics may allow us to significantly increase estimate accuracy.

Acknowledgments

The authors are grateful to Dr. Olli-Pekka Tossavainen for initial discussion on the applicability of the EKF to the discretized LWR model.

References

[1] T. Hey, S. Tansley, K. Tolle (Eds.), The Fourth Paradigm: Data-Intensive Scientific Discovery, Microsoft Research, Redmond, WA, 2009.
[2] J. Kaipio, E. Somersalo, Statistical and Computational Inverse Problems, Springer, New-York, NY, 2005.
[3] F. Bouttier, P. Courtier, Data assimilation concepts and methods, Training course notes of the European Centre for Medium-Range Weather Forecasts, 1999, Reading, UK.
[4] F.-X. Le Dimet, O. Talagrand, Variational algorithms for analysis and assimilation of meteorological observations: theoretical aspects, Tellus A 38 (2) (1986) 97–110.
[5] R. Kalman, A new approach to linear filtering and prediction problems, J. Basic Eng. 82 (1) (1960) 35–45.
[6] N. Wiener, Extrapolation, interpolation, and smoothing of stationary time series with engineering applications, The Technology Press of The Massachusetts Institute of Technology, Boston, MA, 1949.
[7] Y. Bar-Shalom, X. Li, T. Kirubarajan, J. Wiley, Estimation with Applications to Tracking and Navigation, John Wiley and Sons, New York, NY, 2001.
[8] S. Schmidt, Kalman filter: Its recognition and development for aerospace applications, J. Guid. Control 4 (1) (1981) 4–7.
[9] P. Courtier, E. Andersson, W. Heckley, D. Vasiljevic, M. Hamrud, A. Hollingsworth, F. Rabier, M. Fisher, J. Pailleux, The ECMWF implementation of three-dimensional variational assimilation (3D-Var). I: Formulation, Q. J. R. Meteorol. Soc. 124 (550) (1998) 1783–1807.
[10] P. Courtier, J. Thepaut, A. Hollingsworth, A strategy for operational implementation of 4D-Var, using an incremental approach, Q. J. R. Meteorol. Soc. 120 (519) (1994) 1367–1387.
[11] B. Anderson, J. Moore, Optimal Filtering, Prentice Hall, Upper Saddle River, NJ, 1979.
[12] S. Julier, J. Uhlmann, A new extension of the Kalman filter to nonlinear systems, in: Proceedings of AeroSense: SPIE 11th Annual International Symposium on Aerospace/Defense Sensing, Simulation and Controls, Orlando, FL, 1997.
[13] G. Evensen, The ensemble Kalman filter: Theoretical formulation and practical implementation, Ocean Dynam. 53 (4) (2003) 343–367.
[14] J. Liu, R. Chen, Sequential Monte Carlo methods for dynamic systems, J. Amer. Statist. Assoc. 93 (443) (1998) 1032–1044.
[15] R. Chen, J. Liu, Mixture Kalman filters, J. R. Stat. Soc. Ser. B (Stat. Methodol.) 62 (3) (2000) 493–508.
[16] D. Gazis, C. Knapp, On-line estimation of traffic densities from time-series of flow and speed data, Transp. Sci. 5 (3) (1971) 283–301.
[17] M. Szeto, D. Gazis, Application of Kalman filtering to the surveillance and control of traffic systems, Transp. Sci. 6 (4) (1972) 419–439.
[18] Y. Wang, M. Papageorgiou, Real-time freeway traffic state estimation based on extended Kalman filter: a general approach, Transp. Res. 39 (2) (2005) 141–167.
[19] Y. Wang, M. Papageorgiou, A. Messmer, Real-time freeway traffic state estimation based on extended Kalman filter: A case study, Transp. Sci. 41 (2) (2007) 167.
[20] M. Papageorgiou, J.-M. Blosseville, H. Hadj-Salem, Modelling and real-time control of traffic flow on the southern part of Boulevard Peripherique in Paris: Part I: Modelling, Transp. Res. 24 (5) (1990) 345–359.
[21] T. Schreiter, C. van Hinsbergen, F. Zuurbier, H. van Lint, S. Hoogendoorn, Data-model synchronization in extended Kalman filters for accurate online traffic state estimation, in: 2010 Proceedings of the Traffic Flow Theory Conference, Annecy, France, 2010.
[22] S. Smulders, Control of freeway traffic flow by variable speed signs, Transp. Res. 24 (2) (1990) 111–132.
[23] J.-C. Herrera, A. Bayen, Incorporation of lagrangian measurements in freeway traffic state estimation, Transp. Res. 44 (4) (2010) 460–481. http://dx.doi.org/10.1016/j.trb.2009.10.005.

[24] X. Sun, L. Muñoz, R. Horowitz, Mixture Kalman filter based highway congestion mode and vehicle density estimator and its application, in: American Control Conference (ACC), 2004, IEEE, Boston,MA, 2004, pp. 2098–2103.
[25] C. Tampere, L. Immers, An extended Kalman filter application for traffic state estimation using CTM with implicit mode switching and dynamic parameters, in: Intelligent Transportation Systems Conference, 2007. ITSC 2007, Seattle, WA, 2007, pp. 209–216.
[26] C. Daganzo, The cell transmission model: a dynamic representation of highway traffic consistent with the hydrodynamic theory, Transp. Res. 28 (4) (1994) 269–287.
[27] C. Daganzo, The cell transmission model, part II: Network traffic, Transp. Res. 29 (2) (1995) 79–93.
[28] L. Mihaylova, R. Boel, A. Hegyi, Freeway traffic estimation within particle filtering framework, Automatica 43 (2) (2007) 290–300.
[29] D. Work, S. Blandin, O.-P. Tossavainen, B. Piccoli, A. Bayen, A traffic model for velocity data assimilation, Appl. Math. Res. eXpress 1 (1) (2010) 1–35. http://dx.doi.org/10.1093/amrx/abq002.
[30] N. Gordon, D. Salmond, A. Smith, Novel approach to nonlinear/non-Gaussian Bayesian state estimation, in: Radar and Signal Processing, IEE Proceedings F, vol. 140, IET, 1993, pp. 107–113.
[31] L. Mihaylova, R. Boel, A. Hegyi, An unscented Kalman filter for freeway traffic estimation, in: Proceedings of the IFAC Symposium on Control in Transportation Systems, Delft, the Netherlands, 2006, pp. 29–31.
[32] M. Lighthill, G. Whitham, On kinematic waves, II: a theory of traffic flow on long crowded roads, Proc. R. Soc. Lond. 229 (1178) (1956) 317–345.
[33] P. Richards, Shock waves on the highway, Oper. Res. 4 (1) (1956) 42–51.
[34] S. Godunov, A difference method for numerical calculation of discontinuous solutions of the equations of hydrodynamics, Mat. Sb. 89 (3) (1959) 271–306.
[35] L. Evans, Partial Differential Equations, American Mathematical Society, Providence, RI, 1998.
[36] G. Evensen, Inverse methods and data assimilation in nonlinear ocean models, Physica D 77 (1-3) (1994) 108–129.
[37] H. Sorenson, Least-squares estimation: from Gauss to Kalman, Spectrum, IEEE 7 (7) (1970) 63–68.
[38] S. Stigler, Gauss and the invention of least squares, Ann. Stat. (1981) 465–474.
[39] A. Jazwinski, Stochastic Processes and Filtering Theory, Academic Press, New York, NY, 1970.
[40] S. Sherman, Non-mean-square error criteria, IRE Trans. Inform. Theory 4 (3) (1958) 125–126.
[41] Federal Highway Administration, Next Generation Simulation, http://ngsim-community.org/, 2006.
[42] G. Evensen, Using the extended Kalman filter with a multilayer quasi-geostrophic ocean model, J. Geophys. Res. 97 (C11) (1992) 17905–17924.
[43] R. Miller, E. Carter, S. Blue, Data assimilation into nonlinear stochastic models, Tellus A 51 (2) (1999) 167–194.
[44] R. Miller, M. Ghil, F. Gauthiez, Advanced data assimilation in strongly nonlinear dynamical systems, J. Atmospheric Sci. 51 (8) (1994) 1037–1056.
[45] S. Julier, J. Uhlmann, H. Durrant-Whyte, A new method for the nonlinear transformation of means and covariances in filters and estimators, IEEE Trans. Automat. Control 45 (3) (2000) 477–482.
[46] A. Hegyi, D. Girimonte, R. Babuška, B. De Schutter, A comparison of filter configurations for freeway traffic state estimation, in: Intelligent Transportation Systems Conference, 2006, ITSC 2006, Toronto, CA, 2006, pp. 1029–1034.
[47] G. Evensen, Sequential data assimilation with a nonlinear quasi-geostrophic model using Monte Carlo methods to forecast error statistics, J. Geophys. Res. 99 (1994) 10143–10162.
[48] G. Burgers, P. van Leeuwen, G. Evensen, Analysis scheme in the ensemble Kalman filter, Mon. Weather Rev. 126 (6) (1998) 1719–1724.
[49] J. Anderson, An ensemble adjustment Kalman filter for data assimilation, Mon. Weather Rev. 129 (12) (2001) 2884–2903.
[50] C. Andrieu, N. De Freitas, A. Doucet, M. Jordan, An introduction to MCMC for machine learning, J. Mach. Learn. 50 (1) (2003) 5–43.
[51] N. Metropolis, S. Ulam, The Monte Carlo method, J. Amer. Statist. Assoc. 44 (247) (1949) 335–341.
[52] W. Hastings, Monte Carlo sampling methods using Markov chains and their applications, Biometrika 57 (1) (1970).
[53] R. Boel, L. Mihaylova, A compositional stochastic model for real time freeway traffic simulation, Transp. Res. 40 (4) (2006) 319–334.
[54] C. Snyder, T. Bengtsson, P. Bickel, J. Anderson, Obstacles to high-dimensional particle filtering, Mon. Weather Rev. 136 (12) (2008) 4629–4640.
[55] R. Van Der Merwe, A. Doucet, N. De Freitas, E. Wan, The unscented particle filter, Adv. Neural Inform. Process. Syst. 13 (2001) 584–590.
[56] A. Chorin, X. Tu, Implicit sampling for particle filters, Proc. Nat. Acad. Sci. 106 (41) (2009) 17249–17254.
[57] B. Greenshields, A study of traffic capacity, Proc. Highway Res. Board 14 (1) (1935) 448–477.
[58] G. Newell, A simplified theory of kinematic waves in highway traffic, Part II: queueing at freeway bottlenecks, Transp. Res. 27 (4) (1993) 289–303.
[59] T. Li, Nonlinear dynamics of traffic jams, Physica D 207 (1-2) (2005) 41–51.
[60] H. Greenberg, An analysis of traffic flow, Oper. Res. 7 (1) (1959) 79–85.
[61] M. Van Aerde, Single regime speed-flow-density relationship for congested and uncongested highways, in: 74th Annual Meeting of the Transportation Research Board, Washington, DC, 1995.
[62] G. Coclite, M. Garavello, B. Piccoli, Traffic flow on a road network, SIAM J. Math. Anal. 36 (6) (2005) 1862–1886.
[63] H. Holden, N. Risebro, A mathematical model of traffic flow on a network of unidirectional roads, SIAM J. Math. Anal. 26 (4) (1995) 999–1017.
[64] J.-P. Lebacque, First-order macroscopic traffic flow models: Intersection modeling, network modeling, in: Proceedings of the 16th International Symposium on Transportation and Traffic Theory, Flow, Dynamics and Human Interaction, College Park, MD, 2005.
[65] M. Garavello, B. Piccoli, Traffic Flow on Networks, in: American Institute of Mathematical Sciences, Springfield, MO, 2006.
[66] J. Glimm, Solutions in the large for nonlinear hyperbolic systems of equations, Commun. Pure Appl. Math. 18 (1965) 697–715.
[67] R. Leveque, Finite Volume Methods for Hyperbolic Problems, Cambridge University Press, Cambridge, UK, 2002.
[68] A. Bressan, Hyperbolic Systems of Conservation Laws: The One-dimensional Cauchy Problem, Oxford University Press, Oxford, UK, 2000.
[69] C. Claudel, A. Bayen, Lax–hopf based incorporation of internal boundary conditions into hamilton–jacobi equation. part i: Theory, IEEE Trans. Automat. Control 55 (5) (2010) 1142–1157.
[70] C. Claudel, A. Bayen, Lax–hopf based incorporation of internal boundary conditions into hamilton-jacobi equation. part ii: Computational methods, IEEE Trans. Automat. Control 55 (5) (2010) 1158–1174.
[71] P.E. Mazare, A. Dehwah, C.G. Claudel, A.M. Bayen, Analytical and grid-free solutions to the Lighthill–Whitham–Richards traffic flow model, Transp. Res. Part B 45 (10) (2011) 1727–1748.
[72] S. Wong, G. Wong, An analytical shock-fitting algorithm for LWR kinematic wave model embedded with linear speed-density relationship, Transp. Res. 36 (8) (2002) 683–706.
[73] J.-P. Lebacque, The Godunov scheme and what it means for first order macroscopic traffic flow models, in: Proceedings of the 13th International Symposium on Transportation and Traffic Theory, Lyon, France, 1996, pp. 647–677.
[74] H. Payne, Models of freeway traffic and control, Math. Models Public Syst. 1 (1) (1971) 51–61.
[75] G. Whitham, Linear and Nonlinear Waves, John Wiley and Sons, New York, NY, 1974.
[76] A. Aw, M. Rascle, Resurrection of second order models of traffic flow, SIAM J. Appl. Math. 60 (3) (2000) 916–938.
[77] M. Zhang, A non-equilibrium traffic model devoid of gas-like behavior, Transp. Res. 36 (3) (2002) 275–290.
[78] S. Blandin, D. Work, P. Goatin, B. Piccoli, A. Bayen, A general phase transition model for vehicular traffic, SIAM J. Appl. Math. 71 (1) (2011) 107–121. http://dx.doi.org/10.1137/090754467.
[79] R. Colombo, On a 2×2 hyperbolic traffic flow model, Math. Comput. Model. 35 (5-6) (2002) 683–688.
[80] D. Helbing, Improved fluid-dynamic model for vehicular traffic, Phys. Rev. E 51 (4) (1995) 3164–3169.
[81] H. Zhang, Structural properties of solutions arising from a nonequilibrium traffic flow theory, Transp. Res. 34 (7) (2000) 583–603.
[82] C. Huang, Y. Fallah, R. Sengupta, H. Krishnan, Adaptive intervehicle communication control for cooperative safety systems, IEEE Netw. 24 (1) (2010) 6–13.
[83] X. Sun, L. Muñoz, R. Horowitz, Highway traffic state estimation using improved mixture Kalman filters for effective ramp metering control, in: Proceedings of the 42nd IEEE Conference on Decision and Control, Maui, HI, 2003, pp. 6333–6338.
[84] M. Bocquet, C. Pires, L. Wu, Beyond Gaussian statistical modeling in geophysical data assimilation, Mon. Weather Rev. 138 (2010) 2997–3023.
[85] J. Chandrasekar, A. Ridley, D. Bernstein, A comparison of the extended and unscented Kalman filters for discrete-time systems with nondifferentiable dynamics, in: American Control Conference, ACC, 2007, pp. 4431–4436.
[86] M. Cunha, F. Dorini, Statistical moments of the solution of the random Burgers-Riemann problem, Math. Comput. Simulation 79 (5) (2009) 1440–1451.
[87] J. Huttunen, J. Kaipio, Approximation errors in nonstationary inverse problems, Inverse Probl. Imaging 1 (1) (2007) 77–93.
[88] J. Huttunen, J. Kaipio, Approximation error analysis in nonlinear state estimation with an application to state-space identification, Inverse Problems 23 (2007) 2141–2157.
[89] O.-P. Tossavainen, J. Percelay, M. Stacey, J. Kaipio, A. Bayen, State estimation and modeling error approach for 2D shallow water equations and Lagrangian measurements, Water Resources Research 47 (10) (2011) W10510.